3D Non-Stationary Wideband UAV-to-Ground MIMO Channel Models Based on Aeronautic Random Mobility Model

Ji Bian, *Member, IEEE*, Cheng-Xiang Wang, *Fellow, IEEE*, Yu Liu, *Member, IEEE*, Jie Tian, *Member, IEEE*, Jingping Qiao, *Member, IEEE*, and Xiangwei Zheng

***Abstract*—A commonly used assumption in the existing unmanned aerial vehicle (UAV) channel models is that the UAV flies along linear trajectories. However, this assumption does not always hold in realistic UAV communication scenarios. In this paper, we relax the linear trajectory restriction and present a temporally non-stationary channel model for UAV-to-ground communication scenario. The temporal non-stationarity of the channel stemming from time-varying heading directions of the UAV is properly modeled. This is achieved by combining a geometry-based stochastic model (GBSM) and an aeronautic random mobility model (RMM), which is introduced to characterize the movement pattern of UAVs. Based on UAV and ground station (GS) trajectories, time-varying model parameters and statistics including space-time-frequency correlation function (STF-CF), Doppler power spectrum density (PSD), delay PSD, and stationary interval are derived. The influences of the RMM-related parameters on the statistics are presented and analyzed. Some of those statistics are verified by measurements, showing the practicability of the model. The work presented in this paper is helpful in designing UAV communication system considering realistic UAV trajectories.**

***Index Terms*—Channel modeling, non-stationary UAV channels, GBSM, random trajectories, statistical properties.**

Manuscript received March 1, 2021; revised July 3, 2021 and August 17, 2021; accepted September 20, 2021. Date of publication October 1, 2021; date of current version November 18, 2021. This work was supported in part by the National Key R&D Program of China under Grant 2018YFB1801101, in part the National Natural Science Foundation of China (NSFC) under Grants 61960206006, 61901109, 61901247, 61801278, and 62001269, in part by the Shandong Provincial Natural Science Foundation under Grants ZR2020QF001 and ZR2019BF04, in part by the Fundamental Research Funds of Shandong University under Grant 2020GN032, in part by the Frontiers Science Center for Mobile Information Communication and Security, the High Level Innovation and Entrepreneurial Research Team Program in Jiangsu, the High Level Innovation and Entrepreneurial Talent Introduction Program in Jiangsu, the Research Fund of National Mobile Communications Research Laboratory, Southeast University under Grants 2020B01 and 2021B02, in part by the Fundamental Research Funds for Central Universities under Grant 2242021R30001, in part by the Shandong Provincial Scientific Research Programs in colleges and universities under Grant J18KA310, and in part by the Huawei Cooperation Project, the Taishan Scholar Program of Shandong Province, and the EU H2020 RISE TESTBED2 Project under Grant 872172. The review of this article was coordinated by Prof. Sinem Coleri. *(Corresponding author: Cheng-Xiang Wang.)*

Ji Bian, Jie Tian, Jingping Qiao, and Xiangwei Zheng are with the School of Information Science and Engineering, Shandong Normal University, Jinan, Shandong 250358, China (e-mail: jibian@sdnu.edu.cn; tianjiesdu@gmail.com; qiaojingping07@gmail.com; xwzhengcn@163.com).

Cheng-Xiang Wang is with the National Mobile Communications Research Laboratory, School of Information Science and Engineering, Southeast University, Nanjing 210096, China and also with Purple Mountain Laboratories, Nanjing 211111, China (e-mail: chxwang@seu.edu.cn).

Yu Liu is with the School of Microelectronics, Shandong University, Jinan, Shandong 250101, China (e-mail: yuliu@sdu.edu.cn).

Digital Object Identifier 10.1109/TVT.2021.3116953

I. Introduction

The sixth generation (6G) wireless networks are deemed to support ubiquitous always-on connectivity. This implies that the future networks have to be seamlessly integrated with terrestrial, satellite, and airborne networks [1]. Benefitting from cost-effective and high-mobility advantages, unmanned aerial vehicle (UAV) communication techniques are drawing increasing attention from both military and civil fields [2]. UAVs can provide fast deployment of communication networks for diverse application scenarios, e.g., search-and-rescue, disaster monitoring, border surveillance, traffic control, etc. Different from terrestrial nodes, UAVs can fly in the sky dynamically and stay at different heights, which mean the effects of elevation angles relative to the ground should be fully considered in UAV channel modeling [3]. Besides, high-mobility and different multipath characteristics make UAV channels different from the terrestrial ones [4]. Since testing and performance evaluation of communication networks critically depend on the corresponding channel models, accurate and computationally-efficient UAV channel models which can faithfully capture the underlying channel properties are urgently needed.

A. Related Works

According to the modeling approach, the existing UAV channel models can be divided into deterministic and stochastic models. Deterministic models are often developed based on ray-tracing [5]–[7]. In [5], multipath parameters including power, delay, and delay spread of air-to-ground (A2G) channel were estimated by ray-tracing. Similarly, using ray-tracing method, the dependence between altitude of UAV and delay spread of A2G channels was investigated in [6]. In [7], the UAV-to-ship wireless channel was studied via ray-tracing by reconstructing the waves propagating over sea surface between an UAV and a ship. In general, deterministic models are relatively highly accurate but lead to large computation complexity. Besides, they require detail information of propagation environments, such as size and distribution of scatterers and electrical characteristic of materials, which make the deterministic models site-specific.

The stochastic UAV channel models can be divided into geometry-based stochastic models (GBSM) and non-geometrical stochastic models (NGSMs) [8]. In NGSMs, the tapped-delay line (TDL) models were widely adopted for UAV scenarios due to their simple structure [9]–[11]. In [9] and [10], TDL models with nine taps were presented for A2G mountainous and suburban scenarios, respectively. Similarly, a TDL model with three taps was proposed in [11] for A2G over-water scenario. Those TDL models were composed of classic two-ray propagation and additional intermittent multipath components (MPCs). The statistics of each tap were empirically described based on measurements. In [12], A2G channel measurements were conducted at 2 GHz and indicated that the low elevation A2G channel can be studied by the Loo model. Besides, a narrowband channel simulator was presented having the ability to mimic the fading statistics of the UAV channel. The fidelity of those NGSMs relies on accurately estimating stationary interval of the UAV channels. Compared with GBSMs, NGSMs with relatively few adjustable parameters may not fully represent the spatial-temporal characteristics of UAV channels.

The GBSMs are established based upon a large number of rays scattered/reflected by objects distributed stochastically according to certain geometrical shapes. In [13], the A2G channel was modeled by a 3D single-sphere model, in which the scatterers were located on a sphere with the terrestrial user in the center. The aircraft was free of local scattering due to the high altitudes. Similarly, in [14], a channel model for high-altitude platform multiple-input multiple-output (MIMO) communication scenarios was developed. The scatterers distribution was described by a cylinder centering around the ground station (GS). The space-time correlation function (CF) of the proposed model was obtained and analyzed. Similar researches can be found in [15], where an A2G channel model was proposed based on the geometrical cylinder model. In [16], the elliptic-cylinder model was adopted to depict the roadside environments around the low-altitude UAV and GS. In [17], an A2G channel model was developed by assuming that the air station and GS located at the foci of an ellipsoid. The scatterers were filled in the region which is bounded by ellipsoid, ground plane, and average height of the buildings around GS. The angles of arrival (AoAs) were derived based on the geometry. Furthermore, an A2G channel model was presented in [18] and [19] based on a two-cylinder model, which was used to describe the scatterers around the UAV and GS. Channel statistics, e.g., spatial CF, temporal CF, and Doppler power spectral density (PSD) were obtained.

By assuming certain geometric distributions of scatterers, GBSMs can help in obtaining space-time characteristics of UAV channels [20]. Besides, channel measurements have revealed that the wide-sense stationary (WSS) condition of UAV channels is only valid for short distances, which means the time variations of channel parameters and statistics should be faithfully modeled [3]. However, only a few UAV channel models have taken the temporal non-stationarity into consideration. In [21], a temporally non-stationary A2G channel model was presented by extending the geometrical cylinder model with time-varying angular parameters. However, only space-time-frequency CF (STF-CF) and Doppler PSD were investigated. A general A2G channel model was developed in [22], which combines a cylinder model with truncated ellipsoid models. Parameters including cluster number, delay, power, and angles of MPC can evolve over time. Furthermore, based on [14], an A2G channel model for millimeter wave (mmWave) massive MIMO aerial channels was proposed in [23]. The temporal and spatial non-stationarities introduced by the motions of aircraft and large array were modeled. However, the temporal non-stationarities in [21]–[23] were simulated by substituting time-varying Doppler frequencies for traditional time-invariant ones, which makes the path phases inaccurate and lack of physical soundness. The above-mentioned UAV channel models are summarized and compared in Table I.

B. Motivations

As is well-known, a realistic channel model should have the ability of capturing channel properties which relate with the performance of communication systems. For the UAV communication scenarios, the aircraft can move in the 3D space along diverse trajectories. For example, an UAV hovers in the air when used as a cellular base station. A linear trajectory can be found in cargo and transportation applications. In search and rescue, the UAV flies around the possible location of the victim in circular trajectories. In patrolling and reconnaissance missions where a certain target may not be available, highly-dynamic movement patterns with flexible trajectories can be observed. However, the above-mentioned UAV channel models were designed assuming linear trajectory, which may be inconsistent with realistic propagation environments and unable to capture certain channel characteristics resulting from time-varying moving directions of UAVs.

It is worth noting that in [24] and [26], temporally non-stationary GBSMs for A2G and terrestrial mobile-to-mobile (M2M) scenarios were presented, where the heading direction of the aircraft was allowed to change linearly, resulting in a circular trajectory. However, this oversimplified moving trajectory may not flexible enough to capture movement patterns of UAVs. In the field of mobile ad hoc network (MANET) researches, the random mobility models (RMMs) are widely used as foundations for designing and evaluating of system performance, since they can represent the mobility features of mobile nodes [27]. In [25] and [28], GBSMs for air-to-air (A2A) and terrestrial M2M communication scenarios were developed, where the mobile node movements were described by Gauss-Markov RMM. However, the parameters of MPC, e.g., delay and angles, were assumed to be time-invariant, which may be insufficient to simulate the temporal non-stationarity of the channel. Besides, Gauss-markov RMM was designed for ground nodes, whose mobility features are much different from those of aircrafts due to the mechanical and aerodynamic constraints. For example, ground nodes can easily make sharp turns and change speeds abruptly. However, the aircrafts, especially fixed-wing aircrafts, are prone to maintain constant direction and make turns smoothly. As discussed in [29] and [30], ground-based models such as Gauss-Markov RMM cannot reflect kinematic behaviours of aircrafts and may generate misleading results in

TABLE I
IMPORTANT UAV CHANNEL MODELS

Ref.	Modeling Approach	Time Non-WSS	Wideband	Trajectory modeling
[5]	ray-tracing	no	yes	circular
[6], [7]	ray-tracing	no	yes	linear
[9]–[11]	NGSM: TDL model	no	yes	linear
[12]	NGSM: Loo model	no	no	linear
[13]	GBSM: single-sphere model	no	no	linear
[17]	GBSM: truncated ellipsoid model	no	no	linear
[14], [15]	GBSM: single-cylinder model	no	no	linear
[18], [19]	GBSM: two-cylinder model	no	no	linear
[16]	GBSM: elliptic-cylinder model	no	yes	linear
[21]	GBSM: concentric-cylinders model	yes	yes	linear
[23]	GBSM: multiple-cylinders model	yes	yes	linear
[22]	GBSM:cylinder and confocal truncated ellipsoid models	yes	yes	linear
[24]	GBSM: twin-cluster model	yes	yes	circular
[25]	GBSM: single-cylinder model	yes	yes	Gauss-Markov

system performance evaluation. The aforementioned limitations suggest a need to develop temporally non-stationary UAV channel models considering realistic UAV trajectories.

C. Contributions

This paper provides a temporally non-stationary A2G MIMO channel model for UAV communication scenarios. Based on an aeronautic RMM, the proposed model with large amounts of random UAV trajectories can be used in designing and evaluating airborne networks. Besides, for specific scenarios, predefined UAV trajectories can be deterministically generated by using fixed RMM parameters. The major contributions of this paper are listed as follows.

1) A temporally non-stationary UAV-to-ground channel model is presented by introducing an aeronautic RMM into a GBSM. By relaxing the widely used straight-line trajectory assumption, the UAV is allowed to move along realistic trajectories under aerodynamic constraint. The effects of unique mobility features of UAV, such as straight-line moving tendency and smooth turns with large radii can be characterized by the proposed channel model.
2) Time-varying model parameters including delays and angles of MPCs are derived, which are different from those of traditional UAV GBSMs assuming linear trajectories. Considering the time-varying Doppler frequencies, continuity of the path phases is achieved, which describes the temporal non-stationarity of the channel accurately.
3) Expressions of STF-CF, Doppler PSD, and delay PSD of the proposed UAV-to-ground reference model and simulation model are derived. A novel stationary interval metric is proposed and is shown to be useful for capturing the channel non-stationarity resulting from dynamic UAV movements.
4) The impacts of RMM parameters controlling the shape and randomness of UAV trajectories, on channel statistics are presented and analyzed. The consistency among reference model, simulation model, and simulation results ensures the correctness of derivations. The practicability of the model is validated by measurement data.

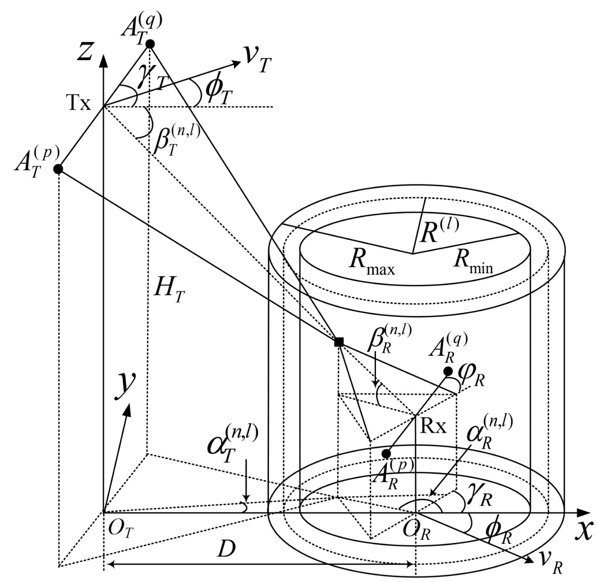

Fig. 1. The proposed temporally non-stationary GBSM for UAV-to-ground MIMO channels.

The remainder of this paper is organized as follows. Section II describes the novel reference UAV channel model, including geometric construction and time-varying model parameters. Key statistics are presented and studied in Section III. Section IV briefly introduces the corresponding simulation model. Numerical results are presented and discussed in Section V. Conclusions are finally drawn in Section VI.

II. 3D WIDEBAND TEMPORALLY NON-STATIONARY UAV-TO-GROUND REFERENCE CHANNEL MODEL

Fig. 1 illustrates the proposed $M_R \times M_T$ UAV-to-ground channel model. Both the UAV and GS are equipped with uniform linear arrays spaced with δ_T and δ_R, respectively. The UAV can move in 3D space with a speed of $v_T = \sqrt{v_{T,xy}^2 + v_{T,z}^2}$, where $v_{T,xy}$ and $v_{T,z}$ are horizontal and vertical speeds of the UAV. Angle ϕ_T describes the moving direction of the UAV in the xy plane, ζ_T is the elevation angle of the moving direction relative to the xy plane. More detailed information of the UAV movements

TABLE II
SUMMARY OF KEY PARAMETER DEFINITIONS

Parameter	Definition
D	Distance between the points directly beneath the UAV and the GS
H_T	Height of the UAV antenna array
$R^{(l)}$	Radius of the lth cylinder
$A_T^{(p)}$, $A_R^{(q)}$	The pth UAV antenna element and the qth GS antenna element, respectively
M_T, M_R	Numbers of UAV and GS antenna elements, respectively
δ_T, δ_R	Antenna spacings of the UAV and GS antenna arrays, respectively
γ_T, γ_R	Tilt angles of the UAV and GS antenna arrays in the xy plane, respectively
φ_R	Elevation angles of the GS antenna array relative to the xy plane
υ_T, ζ_T, ϕ_T	Speed, travel azimuth angle, travel elevation angle of the UAV, respectively
$\upsilon_{T,xy}$, $\upsilon_{T,z}$	Horizontal and vertical speeds of the UAV, respectively
υ_R, ϕ_R	Speed and travel azimuth angle of the GS, respectively
$\alpha_T^{(n,l)}, \beta_T^{(n,l)}$	AAoD and EAoD of the waves impinging on $S^{(n,l)}$, respectively
$\alpha_R^{(n,l)}, \beta_R^{(n,l)}$	AAoA and EAoA of the waves traveling from $S^{(n,l)}$, respectively
$\alpha_T^{\text{LoS}}, \beta_T^{\text{LoS}}, \alpha_R^{\text{LoS}}, \beta_R^{\text{LoS}}$	AAoD, EAoD, AAoA, and EAoA of the LoS path, respectively

can be found in Section II-A. The movements of the GS are confined in the horizontal plane and characterized by the speed υ_R and moving direction ϕ_R. In typical communication scenarios, the UAV flies above rooftops with a height of H_T and is free of local scattering. The scattering environment around the GS is described by a single concentric-cylinders model. Specifically, scatterers, e.g., buildings and vegetation, are spread over the region between cylinders with radii R_{min} and R_{max}. Assuming that there are $N^{(l)}$ scatterers locate on the lth ($l = 1, \ldots, L$) cylinder, whose radius is $R^{(l)}$. The nth ($n = 1, \ldots, N^{(l)}$) scatterer on the lth cylinder is denoted as $S^{(n,l)}$. At initial moment, the projections of transmit and receive antenna array centers on the xy plane, i.e., O_T and O_R, are aligned along the x axis. The distance between O_T and O_R is D. Symbols γ_T and γ_R describe the orientations of the transmit and receive antenna arrays in the xy plane, respectively. Furthermore, φ_R is the elevation angle of the receive antenna array with respect to the xy plane. The azimuth and elevation angles of departure (AAoD and EAoD) of the ray transmitted from the Tx impinging on the scatterer $S^{(n,l)}$ are denoted by $\alpha_T^{(n,l)}$ and $\beta_T^{(n,l)}$, respectively. Similarly, $\alpha_R^{(n,l)}$ and $\beta_R^{(n,l)}$ stand for the azimuth AoA (AAoA) and elevation AoA (EAoA) of the ray received at Rx associated with $S^{(n,l)}$, respectively. Parameters relative to the proposed model are summarized in Table II.

A. RMM for Airborne Networks

In UAV communications, the aircraft can experience dynamic trajectories associated with a wide range of application scenarios. The high-mobility feature of the aircraft introduces temporal non-stationarity of the channel, which should be faithfully represented by UAV channel models [11]. In order to address this challenge, a RMM that can capture various mobility patterns of the aircraft is indispensable. Here, an aeronautic RMM called smooth turn (ST)-RMM is introduced to describe the dynamic trajectories of the aircraft [29]. The ST-RMM was developed based on large numbers of aerial target tracking and has been validated by real flight trajectories [31], [32]. As shown in Fig. 2, the basic principle of the ST-RMM is that the aircraft flies around a point located at the line perpendicular to its moving

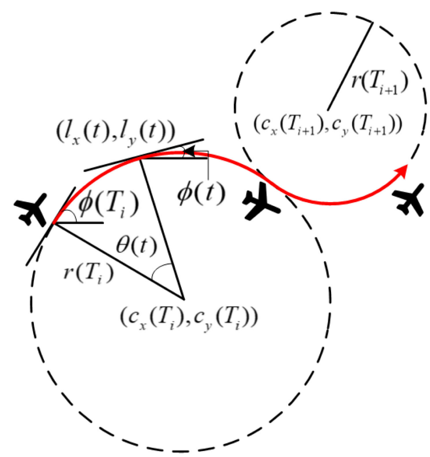

Fig. 2. The ST-RMM for airborne networks.

direction until it chooses another turning center. The dynamics of ST-RMM during the travel time interval $T_i \leqslant t \leqslant T_{i+1}$ $(i = 0, 1, 2, \ldots)$ is given by [29]

$$a_{xyt}(t) = 0 \tag{1}$$

$$a_{xyn}(t) = \frac{v_{xy}^2(t)}{r(T_i)} \tag{2}$$

$$\dot{\phi}_{xy}(t) = -\omega(t) = -v_{xy}(t)/r(T_i) \tag{3}$$

$$\dot{l}_x(t) = v_x(t) = v_{xy}(t)\cos(\phi(t)) \tag{4}$$

$$\dot{l}_y(t) = v_y(t) = v_{xy}(t)\sin(\phi(t)) \tag{5}$$

$$\dot{l}_z(t) = v_z(t) \tag{6}$$

where "$\cdot$" stands for the first-order derivative, $a_{xyt}(t)$ and $a_{xyn}(t)$ are the horizontal tangential and centripetal accelerations of the aircraft at time t, respectively. Symbols $l_x(t)$, $l_y(t)$, and $l_z(t)$ are the coordinates of the aircraft, $v_x(t)$, $v_y(t)$, and $v_z(t)$ are velocity components on x, y, and z axes, respectively. Note that the subscripts "T" on velocity components are omitted for simplicity. Furthermore, $\phi(t)$, and $\omega(t)$ are the heading direction and angular velocity of the aircraft, respectively. During the travel time interval $[T_i, T_{i+1})$, the aircraft moves around a fixed turning center $(c_x(T_i),\ c_y(T_i))$ with a constant turning radius $r(T_i)$. The reciprocal of the turning radii, i.e., $1/r(T_i)$, follow the Gaussian distribution with zero mean and variance σ_s^2, which results in a linear movement tendency and avoids very sharp turns. Note that the turning radii $r(T_i) > 0$ indicates right turns and $r(T_i) < 0$ results in left turns. The travel time interval between T_i and T_{i+1}, i.e., $\tau_i = T_{i+1} - T_i$, is modeled by the exponential distribution with mean $1/\lambda_s$. Note that for the entire trajectory, the line connecting the turning center and the aircraft is perpendicular to the moving direction, ensuring smoothness of the trajectory.

The ST-RMM is flexible to capture diverse movements of the aircraft. For example, imposing $\sigma_s \to 0$ leads to an infinite turning radius, which generates a straight line trajectory. Increasing σ_s results in large angular speeds of the aircraft and more curving trajectories can be generated. Besides, by setting $\lambda_s \to 0$ and $\sigma_s > 0$, the travel time interval τ_i becomes infinite, leading to a circular trajectory. A large value of λ_s means the aircraft changes its turning center frequently, resulting in more wavy trajectories. Moreover, setting $v_z(t) > 0$ means the aircraft is climbing and $v_z(t) < 0$ indicates a descending motion. By setting appropriate parameters, the ST-RMM is able to generate large mounts of trajectories corresponding to different UAV scenarios such as transportation, search and rescue, patrolling, take-off, landing, etc.

B. Channel Impulse Response

The channel impulse response from the pth transmit antenna $A_T^{(p)}$ to the qth receive antenna $A_R^{(q)}$ is calculated as the summation of the line-of-sight (LoS) component and non-LoS (NLoS) components, i.e.,

$$h_{pq}(t,\tau) = h_{pq}^{\rm LoS}(t,\tau) + h_{pq}^{\rm NLoS}(t,\tau) \tag{7}$$

where $h_{pq}^{\rm LoS}(t,\tau)$ and $h_{pq}^{\rm NLoS}(t,\tau)$ are expressed as

$$\begin{aligned} h_{pq}^{\rm LoS}(t,\tau) &= \sqrt{\frac{K\Omega_{pq}}{K+1}} e^{-j\frac{2\pi}{\lambda}\epsilon_{pq}} \\ &\times e^{j\frac{2\pi}{\lambda}v_T t[\cos\zeta_T\cos\beta_T^{\rm LoS}\cos(\alpha_T^{\rm LoS}-\phi_T)+\sin\zeta_T\sin\beta_T^{\rm LoS}]} \\ &\times e^{j\frac{2\pi}{\lambda}v_R t\cos(\alpha_R^{\rm LoS}-\phi_R)\cos\beta_R^{\rm LoS}}\delta(\tau-\tau^{\rm LoS}) \end{aligned} \tag{8}$$

$$\begin{aligned} h_{pq}^{\rm NLoS}(t,\tau) &= \sqrt{\frac{\Omega_{pq}}{K+1}} \lim_{N\to\infty}\frac{1}{\sqrt{N}}\sum_{l=1}^{L}\sum_{n=1}^{N^{(l)}} e^{j\psi^{(n,l)}} \\ &\times e^{j\frac{2\pi}{\lambda}v_T t[\cos(\alpha_T^{(n,l)}-\phi_T)\cos\zeta_T\cos\beta_T^{(n,l)}+\sin\zeta_T\sin\beta_T^{(n,l)}]} \\ &\times e^{j\frac{2\pi}{\lambda}v_R t\cos(\alpha_R^{(n,l)}-\phi_R)\cos\beta_R^{(n,l)}} \\ &\times e^{-j\frac{2\pi}{\lambda}(\epsilon_{p,nl}+\epsilon_{nl,q})}\delta(\tau-\tau^{(n,l)}). \end{aligned} \tag{9}$$

In (8) and (9), $\delta(\cdot)$ stands for Dirac delta function, K denotes the Ricean factor, $\lambda = c/f_c$ is the wavelength, where c designates the speed of light and f_c stands for the carrier frequency. Besides, $N = \sum_{l=1}^{L} N^{(l)}$, ϵ_{pq}, $\epsilon_{p,nl}$, and $\epsilon_{nl,q}$ account for the distances of $A_T^{(p)}$–$A_R^{(q)}$, $A_T^{(p)}$–$S^{(n,l)}$, and $S^{(n,l)}$–$A_R^{(q)}$ links, respectively. Symbol $\tau^{\rm LoS}$ designates the delay of the LoS component and $\tau^{(n,l)}$ accounts for the delay of the ray associated with $S^{(n,l)}$, Ω_{pq} is the transmitted power between $A_T^{(p)}$ and $A_R^{(q)}$, $\psi^{(n,l)}$ is an initial random phase uniformly distributed within $[-\pi,\pi)$.

Note that the cylinder radii are much larger than antenna spacings δ_T and δ_R, i.e., $R_{\min} \gg \max\{\delta_T,\delta_R\}$. Based on the plane wavefront assumption, the travel distances $\epsilon_{p,nl}$, $\epsilon_{nl,q}$, and ϵ_{pq} are calculated as

$$\epsilon_{p,nl} \approx [\varepsilon_{T,nl} - \Delta_T\cos(\alpha_T^{(n,l)}-\gamma_T)]/\cos\beta_T^{(n,l)} \tag{10}$$

$$\epsilon_{nl,q} \approx [R^{(l)} - \Delta_R\cos\varphi_R\cos(\gamma_R-\alpha_R^{(n,l)})]/\cos\beta_R^{(n,l)} \tag{11}$$

$$\epsilon_{pq} \approx (D - \Delta_T\cos\gamma_T + \Delta_R\cos\gamma_R\cos\varphi_R)/\cos\beta_R^{\rm LoS} \tag{12}$$

where $\Delta_T = \frac{M_T-2p+1}{2}\delta_T$, $\Delta_R = \frac{M_R-2q+1}{2}\delta_R$, $\varepsilon_{T,nl} = [D^2 + (R^{(l)})^2 + 2DR^{(l)}\cos\alpha_R^{(n,l)}]^{\frac{1}{2}}$. The time delay of the MPCs, i.e., $\tau^{\rm LoS}$ and $\tau^{(n,l)}$, can be calculated as

$$\tau^{\rm LoS} = \frac{\sqrt{D^2+H_T^2}}{c} \tag{13}$$

$$\tau^{(n,l)} = \frac{\varepsilon_{T,nl}}{c\cdot\cos\beta_T^{(n,l)}} + \frac{R^{(l)}}{c\cdot\cos\beta_R^{(n,l)}}. \tag{14}$$

For the NLoS components, the AoDs and AoAs of the waves are interdependent. The interrelationship between them can be expressed as

$$\alpha_T^{(n,l)} = \arcsin\left(\frac{R^{(l)}\sin\alpha_R^{(n,l)}}{\varepsilon_{T,nl}}\right) \tag{15}$$

$$\beta_T^{(n,l)} = \arctan\left(\frac{R^{(l)}\tan\beta_R^{(n,l)} - H_T}{\varepsilon_{T,nl}}\right). \tag{16}$$

C. Time-Varying Model Parameters

In this model, both the aircraft and GS are in motion, which makes the model temporally non-stationary. The movement of the aircraft is described using the 3D ST-RMM and the GS is assumed to move along a straight line. According to the movements of UAV and GS, the model is extended by deriving the time-evolution of model parameters.

Based on the geometry, $\alpha_T^{(n,l)}(t)$ and $\beta_T^{(n,l)}(t)$ of the wave impinging on $S^{(n,l)}$ during the travel time interval $[T_i, T_{i+1})$ can be calculated as

$$\alpha_T^{(n,l)}(t) = \arctan\left(\frac{R^{(l)}\sin\alpha_R^{(n,l)} - l_y(t)}{D + R^{(l)}\cos\alpha_R^{(n,l)} - l_x(t)}\right) \tag{17}$$

$$\beta_T^{(n,l)}(t) = \arctan\left(\frac{R^{(l)}\tan\beta_R^{(n,l)} - l_z(t)}{\varepsilon_{T,n}(t)}\right) \tag{18}$$

where $\varepsilon_{T,n}(t) = [(R^{(l)}\sin\alpha_R^{(n,l)} - l_y(t))^2 + (\xi_{T,nl} - l_x(t))^2]^{1/2}$. For simplicity, $v_{T,xy}(t)$ and $v_{T,z}(t)$ are assumed to be constant over time. Thus, $l_z(t) = H_T + v_{T,z}t$, $l_x(t)$ and $l_y(t)$ are determined as [29]

$$l_x(t) = c_x(T_i) - r(T_i)\sin\phi_T(t) \tag{19}$$

$$l_y(t) = c_y(T_i) + r(T_i)\cos\phi_T(t) \tag{20}$$

where

$$\phi_T(t) = \phi_T(T_i) - \theta(t) - 2\pi \left\lfloor \frac{\phi_T(T_i) - \theta(t)}{2\pi} \right\rfloor \quad (21)$$

$$\theta(t) = \frac{v_{T,xy}}{r(T_i)}(t - T_i) \quad (22)$$

where $\lfloor \cdot \rfloor$ denotes the floor function.

For the next travel time interval, i.e., $[T_{i+1}, T_{i+2})$, the time-varying AAoDs and EAoDs are calculated according to the turning radius $r(T_{i+1})$ and the new turning center $(c_x(T_{i+1}), c_y(T_{i+1}))$. The x and y coordinates of the new turning center during $[T_{i+1}, T_{i+2})$ are determined as

$$c_x(T_{i+1}) = c_x(T_i) + [r(T_{i+1}) - r(T_i)] \sin\left(\phi(T_i) - \frac{v_{T,xy}(t)\cdot\tau_i}{r(T_i)}\right) \quad (23)$$

$$c_y(T_{i+1}) = c_y(T_i) - [r(T_{i+1}) - r(T_i)] \cos\left(\phi(T_i) - \frac{v_{T,xy}(t)\cdot\tau_i}{r(T_i)}\right). \quad (24)$$

Proof: Based on (19), the x coordinate of the turning center, i.e., $c_x(T_{i+1})$ $(T_{i+1} \leqslant t < T_{i+2})$ can be express as

$$\begin{aligned} c_x(T_{i+1}) &= l_x(t) + r(T_{i+1}) \sin\phi_T(t) \\ &= l_x(T_{i+1}) + r(T_{i+1}) \sin\phi_T(T_i + \tau_i) \end{aligned} \quad (25)$$

Note that the trajectories in adjacent travel time intervals are smoothly connected, we have

$$\begin{aligned} l_x(T_{i+1}) &= l_x(T_i + \tau_i) \\ &= c_x(T_i) - r(T_i)\sin\phi_T(T_i + \tau_i). \end{aligned} \quad (26)$$

Furthermore, the heading direction $\phi_T(T_i + \tau_i)$ can be calculated according to (21) and (22) as

$$\phi_T(T_i + \tau_i) = \phi_T(T_i) - \frac{v_{T,xy}\cdot\tau_i}{r(T_i)} - 2\pi\left\lfloor \frac{\phi_T(T_i)}{2\pi} - \frac{v_{T,xy}\cdot\tau_i}{r(T_i)2\pi} \right\rfloor. \quad (27)$$

By substituting (26) and (27) into (25), we obtain (23). The y coordinate of the turning center, i.e., $c_y(T_{i+1})$ in (24) can be derived following the similar method. ■

For the Rx side, $\alpha_R^{(n,l)}(t)$ has to be derived in two cases and calculated separately, i.e., Case I ($R^{(l)} \sin\alpha_R^{(n,l)} \leqslant v_R t \sin\phi_R$) and Case II ($R^{(l)} \sin\alpha_R^{(n,l)} > v_R t \sin\phi_R$). For ease of analysis, the 2D top-down view of the UAV-to-ground model for the two cases is shown in Fig. 3. The AoAs $\alpha_R^{(n,l)}(t)$ and $\beta_R^{(n,l)}(t)$ of the wave traveling associated with $S^{(n,l)}$ are calculated as

$$\alpha_R^{(n,l)}(t) = \begin{cases} -\arccos\left(\frac{R^{(l)}\cos\alpha_R^{(n,l)} - v_R t\cos\phi_R}{\varepsilon_{nl,R}(t)}\right), \\ R^{(l)}\sin\alpha_R^{(n,l)} \leqslant v_R t \sin\phi_R \\ \arccos\left(\frac{R^{(l)}\cos\alpha_R^{(n,l)} - v_R t\cos\phi_R}{\varepsilon_{nl,R}(t)}\right), \\ R^{(l)}\sin\alpha_R^{(n,l)} > v_R t \sin\phi_R \end{cases} \quad (28)$$

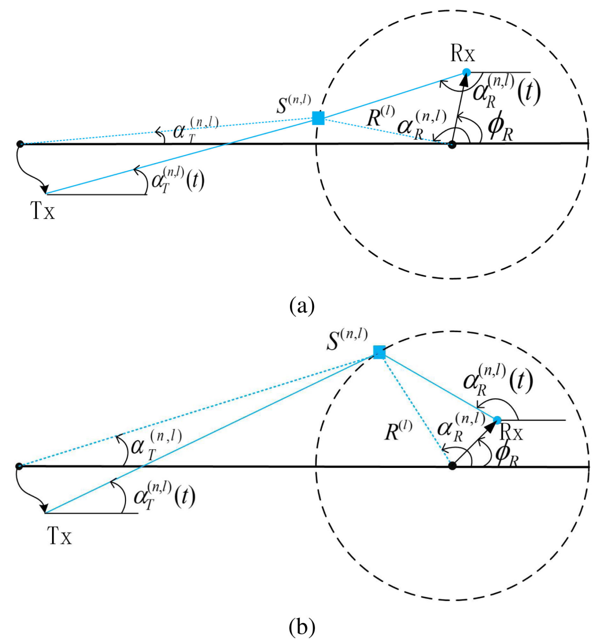

Fig. 3. Top-down view of the UAV-to-ground channel model for (a) Case I ($R^{(l)}\sin\alpha_R^{(n,l)} \leqslant v_R t\sin\phi_R$) and (b) Case II ($R^{(l)}\sin\alpha_R^{(n,l)} > v_R t \sin\phi_R$).

$$\beta_R^{(n,l)}(t) = \arctan\left(\frac{R^{(l)}\tan\beta_R^{(n,l)}}{\varepsilon_{nl,R}(t)}\right) \quad (29)$$

where $\varepsilon_{nl,R}(t) = [(R^{(l)})^2 + (v_R t)^2 - 2R^{(l)} v_R t \cos(\alpha_R^{(n,l)} - \phi_R)]^{1/2}$. Finally, the propagation delay of the wave associated $S^{(n,l)}$ is rewritten as

$$\tau^{(n,l)}(t) = \frac{\varepsilon_{T,nl}(t)}{c\cdot\cos\beta_T^{(n,l)}(t)} + \frac{\varepsilon_{nl,R}(t)}{c\cdot\cos\beta_R^{(n,l)}(t)}. \quad (30)$$

For LoS component, time-varying angles $\alpha_R^{\text{LoS}}(t)$ and $\beta_R^{\text{LoS}}(t)$ are given by

$$\alpha_R^{\text{LoS}}(t) = \arctan\left(\frac{v_R t\sin\phi_R - l_y(t)}{D + v_R t\cos\phi_R - l_x(t)}\right) \quad (31)$$

$$\beta_R^{\text{LoS}}(t) = \arctan\left(\frac{l_z(t)}{\sqrt{[D - l_x(t)]^2 + [l_y(t)]^2}}\right). \quad (32)$$

Besides, the delay of the LoS ray, i.e., $\tau^{\text{LoS}}(t)$, should be recalculated according to the motions of transceiver, i.e.,

$$\tau^{\text{LoS}}(t) = \frac{\sqrt{\begin{matrix} D + v_R t\cos\phi_R - l_x(t)]^2 \\ +[v_R t\sin\phi_R - l_y(t)]^2 \end{matrix}}}{c\cdot\cos\beta_R^{\text{LoS}}(t)}. \quad (33)$$

In addition to the model parameters, the channel impulse responses in (8) and (9) have to be rewritten to ensure the accuracy of the path phases [33]. The new channel impulse responses considering time-varying parameters are written as

$$h_{pq}^{\text{LoS}}(t,\tau) = \sqrt{\frac{K\Omega_{pq}}{K+1}} e^{-j\frac{2\pi}{\lambda}\epsilon_{pq}} e^{j2\pi\int_0^t f_T^{\text{LoS}}(t')\mathrm{d}t'}$$

$$\times e^{j2\pi \int_0^t f_R^{\mathrm{LoS}}(t')\mathrm{d}t'} \delta(\tau - \tau^{\mathrm{LoS}}(t)) \tag{34}$$

$$h_{pq}^{\mathrm{NLoS}}(t,\tau) = \sqrt{\frac{\Omega_{pq}}{K+1}} \lim_{N\to\infty} \frac{1}{\sqrt{N}} \sum_{l=1}^{L} \sum_{n=1}^{N^{(l)}} \times e^{-j\frac{2\pi}{\lambda}(\epsilon_{p,nl}+\epsilon_{nl,q})} e^{j2\pi \int_0^t f_T^{(n,l)}(t')\mathrm{d}t'} \times e^{j2\pi \int_0^t f_R^{(n,l)}(t')\mathrm{d}t'} e^{j\psi^{(n,l)}} \delta(\tau - \tau^{(n,l)}(t)) \tag{35}$$

where $N = \sum_{l=1}^{L} N^{(l)}$, the time-varying Doppler shifts for LoS and NLoS components are given by

$$f_T^{\mathrm{LoS}}(t) = \frac{v_T}{\lambda}[\cos\zeta_T \cos\beta_T^{\mathrm{LoS}}(t)\cos(\alpha_T^{\mathrm{LoS}}(t) - \phi_T(t)) + \sin\zeta_T \sin\beta_T^{\mathrm{LoS}}(t)] \tag{36}$$

$$f_R^{\mathrm{LoS}}(t) = \frac{v_R}{\lambda}\cos(\alpha_R^{\mathrm{LoS}}(t) - \phi_R)\cos\beta_R^{\mathrm{LoS}}(t) \tag{37}$$

$$f_T^{(n,l)}(t) = \frac{v_T}{\lambda}[\cos\zeta_T \cos\beta_T^{(n,l)}(t)\cos(\alpha_T^{(n,l)}(t) - \phi_T(t)) + \sin\zeta \sin\beta_T^{(n,l)}(t)] \tag{38}$$

$$f_R^{(n,l)}(t) = \frac{v_R}{\lambda}\cos(\alpha_R^{(n,l)}(t) - \phi_R)\cos\beta_R^{(n,l)}(t). \tag{39}$$

III. Statistical Properties of the UAV-to-Ground Reference Model

Statistical properties are critical for analyzing the corresponding channel behaviors. The statistical properties presented in this section includes STF-CF, Doppler PSD, and delay PSD. Besides, a novel stationary interval metric based on the time-variation of Doppler PSDs is proposed, which is shown to be useful to characterize channel non-stationarities due to dynamic movements of the UAV.

A. Time-Varying STF-CF

To facilitate analysis, the channel impulse response is converted to channel transfer function as $H_{pq}(t,f) = \mathcal{F}_\tau\{h_{pq}(t,\tau)\}$, where $\mathcal{F}_\tau\{\cdot\}$ indicates the Fourier transform with respect to τ. Therefore, the time-varying STF-CF between $H_{pq}(t,f)$ and $H_{p'q'}(t,f)$ can be written as [34]

$$\rho_{pq,p'q'}(t,\Delta t,\Delta f) = \frac{\mathrm{E}[H_{pq}^*(t,f)H_{p'q'}(t+\Delta t, f+\Delta f)]}{\sqrt{\Omega_{pq}\Omega_{p'q'}}} = \rho_{pq,p'q'}^{\mathrm{LoS}}(t,\Delta t,\Delta f) + \rho_{pq,p'q'}^{\mathrm{NLoS}}(t,\Delta t,\Delta f) \tag{40}$$

where $(\cdot)^*$ is the complex conjugate operation, $\mathrm{E}\{\cdot\}$ denotes the statistical expectation operator, Δt and Δf are time and frequency separations, respectively. Note that the antenna separations, i.e., $\Delta d_T = (p'-p)\delta_T$ and $\Delta d_R = (q'-q)\delta_R$ are represented implicitly by the subscript $pq, p'q'$. Based on (34), we can derive the LoS component of $\rho_{pq,p'q'}(t,\Delta t,\Delta f)$ as

$$\rho_{pq,p'q'}^{\mathrm{LoS}}(t,\Delta t,\Delta f) = \frac{K}{K+1} e^{j\frac{2\pi}{\lambda}(\epsilon_{pq}-\epsilon_{p'q'})} \times e^{j2\pi \int_t^{t+\Delta t} f_T^{\mathrm{LoS}}(t')\mathrm{d}t'} e^{j2\pi \int_t^{t+\Delta t} f_R^{\mathrm{LoS}}(t')\mathrm{d}t'} \times e^{j2\pi f[\tau^{\mathrm{LoS}}(t)-\tau^{\mathrm{LoS}}(t+\Delta t)]} e^{-j2\pi\Delta f \tau^{\mathrm{LoS}}(t+\Delta t)}. \tag{41}$$

By using the following approximations $\cos\beta_R^{\mathrm{LoS}}(t) \approx \frac{D}{\sqrt{H_T^2+D^2}}$, $\alpha_R^{\mathrm{LoS}}(t) \approx \pi$, $\alpha_T^{\mathrm{LoS}}(t) \approx 0$, and $\tau^{\mathrm{LoS}}(t) \approx \frac{\sqrt{H_T^2+D^2}}{c}$, (41) becomes

$$\rho_{pq,p'q'}^{\mathrm{LoS}}(t,\Delta t,\Delta f) \approx \frac{K}{K+1} e^{-j2\pi\frac{\Delta f}{c}\sqrt{H_T^2+D^2}} \times e^{j\frac{2\pi\sqrt{H_T^2+D^2}}{\lambda\cdot D}[(q'-q)\delta_R\cos\varphi_R\cos\gamma_R + (p-p')\delta_T\cos\gamma_T]} \times e^{j\frac{2\pi D}{\lambda\sqrt{H_T^2+D^2}}\left[v_T\cos\zeta_T\int_t^{t+\Delta t}\cos\phi_T(t')\mathrm{d}t' - v_R\cos\phi_R\Delta t\right]} \times e^{-j\frac{2\pi H_T v_T \sin\zeta_T \Delta t}{\lambda\sqrt{H_T^2+D^2}}}. \tag{42}$$

In the reference model, as the quantity of cylinders L and the quantity of scatterers on each cylinder $N^{(l)}$ tend to infinity, the parameters $\alpha_T^{(n,l)}$, $\beta_T^{(n,l)}$, $\alpha_R^{(n,l)}$, $\beta_R^{(n,l)}$, and $R^{(l)}$ become continuous. Thus, we derive the NLoS component of time-varying STF-CF as

$$\rho_{qp,p'q'}^{\mathrm{NLoS}}(t,\Delta t,\Delta f) = \frac{1}{K+1}\int_{R_{\min}}^{R_{\max}}\int_{\beta_1}^{\beta_2}\int_{-\pi}^{\pi} e^{j\frac{2\pi}{\lambda}\left[\frac{(p-p')\delta_T\cos(\alpha_T-\gamma_T)}{\cos\beta_T} + \frac{(q-q')\delta_R\cos\phi_R\cos(\gamma_R-\alpha_R)}{\cos\beta_R}\right]} \times e^{j2\pi\int_t^{t+\Delta t} f_T(t')\mathrm{d}t'} e^{j2\pi\int_t^{t+\Delta t} f_R(t')\mathrm{d}t'} \times e^{-j2\pi\Delta f\tau(t+\Delta t)} e^{j2\pi f[\tau(t)-\tau(t+\Delta t)]} \times p(R)p(\beta_R)p(\alpha_R)\mathrm{d}R\mathrm{d}\beta_R\mathrm{d}\alpha_R. \tag{43}$$

Note that $f_T(t)$ and $f_R(t)$ are Doppler shifts in (38) and (39) with continuous angular parameters, respectively. In the reference model, azimuth angles α_R are described by the von Mises distribution [35], i.e., $p(\alpha_R) = e^{\kappa\cos(\alpha_R-\alpha_\mu)}/[2\pi I_0(\kappa)]$, since it can be simplified to many other widely used scatterer distributions. Here, $\alpha_R \in [-\pi,\pi)$, $I_0(\cdot)$ denotes the zeroth-order modified Bessel function of the first kind, α_μ designates the mean angle, κ indicates the angular spread around α_μ. The elevation angles β_R are modeled by the probability density function (PDF) as $p(\beta_R) = \pi\cos[\pi\beta_R/(2\beta_m)]/(4\beta_m)$, $|\beta_R| \le |\beta_m| \le \frac{\pi}{2}$, where β_m is the maximum value of β_R [36]. Furthermore, the radii of the cylinders R are described as $p(R) = 2R/(R_{\max}^2 - R_{\min}^2)$, $R_{\min} \leqslant R \leqslant R_{\max}$ [37].

B. Time-Varying Doppler PSD

The time-varying Doppler PSD is obtained by applying Fourier transform to the ST-CF, i.e., $S_{pq,p'q'}(t,\nu) = \mathcal{F}_{\Delta t}\{\rho_{pq,p'q'}(t,\Delta t,\Delta f = 0)\}$ [38]. According to (40), the time-varying Doppler PSD is given as

$$S_{pq,p'q'}(t,\nu) = S_{pq,p'q'}^{\mathrm{LoS}}(t,\nu) + S_{pq,p'q'}^{\mathrm{NLoS}}(t,\nu) \tag{44}$$

where $S^{\mathrm{LoS}}_{pq,p'q'}(t,\nu)$ and $S^{\mathrm{NLoS}}_{pq,p'q'}(t,\nu)$ are calculated as

$$S^{\mathrm{LoS}}_{pq,p'q'}(t,\nu) = \int \rho^{\mathrm{LoS}}_{pq,p'q'}(t,\Delta t)e^{-j2\pi\nu\Delta t}\mathrm{d}\Delta t$$
$$\approx \frac{K}{K+1}e^{j\frac{2\pi\sqrt{H_T^2+D^2}}{\lambda\cdot D}[(q'-q)\delta_R\cos\varphi_R\cos\gamma_R+(p-p')\delta_T\cos\gamma_T]}$$
$$\times\,\delta\left(\frac{D\left[v_T\cos\zeta_T\cos\phi_T(t)-v_R\cos\phi_R\right]-H_T v_T\sin\zeta_T}{\lambda\sqrt{H_T^2+D^2}}\right) \tag{45}$$

$$S^{\mathrm{NLoS}}_{pq,p'q'}(t,\nu) = \int \rho^{\mathrm{NLoS}}_{pq,p'q'}(t,\Delta t)e^{-j2\pi\nu\Delta t}\mathrm{d}\Delta t. \tag{46}$$

C. Time-Varying Delay PSD

The time-varying delay PSD is the inverse Fourier transform of frequency correlation function (FCF) with respect to Δf, i.e., $P_{pq,p'q'}(t,\tau) = \mathcal{F}^{-1}_{\Delta f}\{\rho_{qp,p'q'}(t,\Delta t=0,\Delta f)\}$. From (40), the time-varying delay PSD is expressed as

$$P_{pq,p'q'}(t,\tau) = P^{\mathrm{LoS}}_{pq,p'q'}(t,\tau) + P^{\mathrm{NLoS}}_{pq,p'q'}(t,\tau) \tag{47}$$

where $P^{\mathrm{LoS}}_{pq,p'q'}(t,\tau)$ and $P^{\mathrm{NLoS}}_{pq,p'q'}(t,\tau)$ are given as

$$P^{\mathrm{LoS}}_{pq,p'q'}(t,\tau) = \int \rho^{\mathrm{LoS}}_{pq,p'q'}(t,\Delta f)e^{j2\pi\tau\Delta f}\mathrm{d}\Delta f$$
$$\approx \frac{K}{K+1}e^{j\frac{2\pi\sqrt{H_T^2+D^2}}{\lambda\cdot D}[(q'-q)\delta_R\cos\varphi_R\cos\gamma_R+(p-p')\delta_T\cos\gamma_T]}$$
$$\times\,\delta\left(\tau-\sqrt{\frac{H_T^2+D^2}{c}}\right) \tag{48}$$

$$P^{\mathrm{NLoS}}_{pq,p'q'}(t,\tau) = \int \rho^{\mathrm{NLoS}}_{pq,p'q'}(t,\Delta f)e^{j2\pi\tau\Delta f}\mathrm{d}\Delta f. \tag{49}$$

D. Stationary Interval

Most UAV channel models were developed base on the WSS assumption, which simplifies the model construction and statistical analysis. The WSS assumption is valid when observation time is smaller than the stationary interval. However, this is hard to achieve for UAV communication scenarios due to fast-changing properties of UAV channels. Stationary interval can be calculated by estimating the distance or similarity of statistics at two time instants. For example, collinearity was calculated based on two channel correlation matrices [39] or power delay profiles [40] separated by certain time intervals. However, those metrics were designed for terrestrial communication scenarios without considering the effects of dynamic trajectories. Inspired by fact that UAV trajectories can significantly influence Doppler PSDs of UAV channels, the distance between Doppler PSDs at two time instants can be treated as a measure of temporal non-stationarity of UAV channels. The distance between $S_{pq,p'q'}(t_i,\nu)$ and $S_{pq,p'q'}(t_i+\Delta t,\nu)$ can be defined as

$$d_{\mathrm{DPSD}}(t_i,\Delta t) =$$
$$1-\frac{\left|\int S^*_{pq,p'q'}(t_i,\nu)S_{pq,p'q'}(t_i+\Delta t,\nu)\mathrm{d}\nu\right|}{\max\{\int|S_{pq,p'q'}(t_i,\nu)|^2\mathrm{d}\nu,\int|S_{pq,p'q'}(t_i+\Delta t,\nu)|^2\mathrm{d}\nu\}} \tag{50}$$

where $d_{\mathrm{DPSD}}(t_i,\Delta t)\in[0,1]$. It is obvious that $d_{\mathrm{DPSD}}(t_i,\Delta t)$ tends to 0 if two Doppler PSDs are quite similar and becomes 1 when the Doppler PSDs differ to a maximum extent. The stationary interval at time instant t_i is the maximum interval in which $d_{\mathrm{DPSD}}(t_i,\Delta t)$ below threshold c_{thresh}, i.e.,

$$T_c(t_i) = \max\{\Delta t \mid d_{\mathrm{DPSD}}(t_i,\Delta t)\leqslant c_{\mathrm{thresh}}\}. \tag{51}$$

The above equation provides a metric of how rapidly the channel parameters and statistics evolve due to the model geometry changes when the UAV and GS move along certain trajectories. A fast-changing model geometry results in a short stationary interval, beyond which the temporal non-stationarity cannot be neglected.

IV. 3D Wideband Temporally Non-Stationary UAV-to-Ground Simulation Model

A. Channel Impulse Response of the UAV-to-Ground Simulation Model

The reference channel model considers infinite number of rays, which leads to a large computation complexity and makes the model hard to implement. In contrast, the simulation model is established assuming a certain quantity of rays and illustrates similar statistical performances compared with the reference one. The impulse response of the simulation model between $A_T^{(p)}$ and $A_R^{(q)}$ is given by

$$\tilde{h}_{pq}(t,\tau) = \tilde{h}^{\mathrm{LoS}}_{pq}(t,\tau) + \tilde{h}^{\mathrm{NLoS}}_{pq}(t,\tau) \tag{52}$$

where $\tilde{h}^{\mathrm{LoS}}_{pq}(t,\tau)$ and $\tilde{h}^{\mathrm{NLoS}}_{pq}(t,\tau)$ are given by

$$\tilde{h}^{\mathrm{LoS}}_{pq}(t,\tau) = \sqrt{\frac{K\Omega_{pq}}{K+1}}e^{-j\frac{2\pi}{\lambda}\epsilon_{pq}}$$
$$\times\, e^{j\frac{2\pi}{\lambda}v_T t[\cos\zeta_T\cos\beta_T^{\mathrm{LoS}}\cos(\alpha_T^{\mathrm{LoS}}-\phi_T)+\sin\zeta_T\sin\beta_T^{\mathrm{LoS}}]}$$
$$\times\, e^{j\frac{2\pi}{\lambda}v_R t\cos(\alpha_R^{\mathrm{LoS}}-\phi_R)\cos\beta_R^{\mathrm{LoS}}}\delta(\tau-\tau^{\mathrm{LoS}}) \tag{53}$$

$$\tilde{h}^{\mathrm{NLoS}}_{pq}(t,\tau) = \sqrt{\frac{\Omega_{pq}}{K+1}}\frac{1}{\sqrt{N}}\sum_{l=1}^{L}\sum_{n=1}^{N^{(l)}}e^{j\psi^{(n,l)}}$$
$$\times\, e^{j\frac{2\pi}{\lambda}v_T t[\cos(\tilde{\alpha}_T^{(n,l)}-\phi_T)\cos\zeta_T\cos\tilde{\beta}_T^{(n,l)}+\sin\zeta_T\sin\tilde{\beta}_T^{(n,l)}]}$$
$$\times\, e^{j\frac{2\pi}{\lambda}v_R t\cos(\tilde{\alpha}_R^{(n,l)}-\phi_R)\cos\tilde{\beta}_R^{(n,l)}}$$
$$\times\, e^{-j\frac{2\pi}{\lambda}(\epsilon_{p,nl}+\epsilon_{nl,q})}\delta(\tau-\tau^{(n,l)}). \tag{54}$$

It is apparent that the proposed simulation model relies on the discrete parameters, i.e., $\tilde{\alpha}_T^{(n,l)}$, $\tilde{\beta}_T^{(n,l)}$, $\tilde{\alpha}_R^{(n,l)}$, $\tilde{\beta}_R^{(n,l)}$, and $\tilde{R}^{(l)}$. Other parameters are the same as those in reference model. According to the modified method of equal areas (MMEA) [41], the discrete parameters $\tilde{\alpha}_R^{(n,l)}$ are determined by solving the equation

$$\frac{n-1/4}{N^{(l)}} = \int_{-\pi}^{\tilde{\alpha}_R^{(n,l)}} p(\alpha_R)\mathrm{d}\alpha_R \tag{55}$$

and can be further calculated as

$$\tilde{\alpha}_R^{(n,l)} = F^{-1}\left(\frac{n-1/4}{N^{(l)}}\right) \tag{56}$$

where $F^{-1}(\cdot)$ is the inverse cumulative distribution function of AAoA α_R. Following a similar method, the discrete parameters $\tilde{\beta}_R^{(n,l)}$ are obtained as

$$\tilde{\beta}_R^{(n,l)} = \frac{2\beta_m}{\pi}\arcsin\left(\frac{2n-1}{N^{(l)}}-1\right) \tag{57}$$

where $n = 1, 2, \ldots, N^{(l)}$. The discrete parameters $\tilde{\alpha}_T^{(n,l)}$ and $\tilde{\beta}_T^{(n,l)}$ can be determined according the interrelationship between AoAs and AoDs. In addition, the discrete radii $\tilde{R}^{(l)}$ are obtained as

$$\tilde{R}^{(l)} = \sqrt{(l-0.5)(R_{\max}^2 - R_{\min}^2)/L + R_{\min}^2} \tag{58}$$

where $l = 1, 2, \ldots, L$.

B. Statistical Properties of the UAV-to-Ground Simulation Model

The simulation model considers a limited number of rays or scatterers, thereby reducing the model complexity compared with the reference model. In this subsection, statistical properties of the proposed simulation model are presented by replacing continuous model parameters in (40)–(51) with discrete ones, i.e., $\tilde{\alpha}_T^{(n,l)}$, $\tilde{\beta}_T^{(n,l)}$, $\tilde{\alpha}_R^{(n,l)}$, $\tilde{\beta}_R^{(n,l)}$, and $\tilde{R}^{(l)}$. Note that when $L, N^{(l)} \to \infty$, those statistical properties have the same expressions as those of the reference model.

1) Time-Varying STF-CF: The time-varying STF-CF of the simulation model is written as

$$\tilde{\rho}_{pq,p'q'}(t,\Delta t,\Delta f) = \tilde{\rho}_{pq,p'q'}^{\mathrm{LoS}}(t,\Delta t,\Delta f) + \tilde{\rho}_{pq,p'q'}^{\mathrm{NLoS}}(t,\Delta t,\Delta f) \tag{59}$$

where the $\tilde{\rho}_{pq,p'q'}^{\mathrm{LoS}}(t,\Delta t,\Delta f)$ and $\tilde{\rho}_{pq,p'q'}^{\mathrm{NLoS}}(t,\Delta t,\Delta f)$ are given as

$$\begin{aligned}\tilde{\rho}_{pq,p'q'}^{\mathrm{LoS}}(t,\Delta t,\Delta f) &= \frac{K}{K+1} e^{j\frac{2\pi}{\lambda}(\epsilon_{pq}-\epsilon_{p'q'})} \\ &\times e^{j2\pi\int_t^{t+\Delta t} f_T^{\mathrm{LoS}}(t')\mathrm{d}t'} e^{j2\pi\int_t^{t+\Delta t} f_R^{\mathrm{LoS}}(t')\mathrm{d}t'} \\ &\times e^{j2\pi f[\tau^{\mathrm{LoS}}(t)-\tau^{\mathrm{LoS}}(t+\Delta t)]} e^{-j2\pi\Delta f\tau^{\mathrm{LoS}}(t+\Delta t)}\end{aligned} \tag{60}$$

$$\begin{aligned}&\tilde{\rho}_{qp,p'q'}^{\mathrm{NLoS}}(t,\Delta t,\Delta f) \\ &= \frac{1}{(K+1)N}\sum_{l=1}^{L}\sum_{n=1}^{N^{(l)}} e^{j\frac{2\pi}{\lambda}(\epsilon_{p,nl}-\epsilon_{p,'nl}+\epsilon_{nl,q}-\epsilon_{nl,q'})} \\ &\times e^{j2\pi\int_t^{t+\Delta t} f_T^{(n,l)}(t')\mathrm{d}t'} e^{j2\pi\int_t^{t+\Delta t} f_R^{(n,l)}(t')\mathrm{d}t'} \\ &\times e^{-j2\pi\Delta f\tau^{(n,l)}(t+\Delta t)} e^{j2\pi f[\tau^{(n,l)}(t)-\tau^{(n,l)}(t+\Delta t)]}\end{aligned} \tag{61}$$

where $N = \sum_{l=1}^{L} N^{(l)}$.

TABLE III
PARAMETERS OF THE ST-RMM TAKEN BY THE AIRCRAFT

Trajectory	Parameters
I	$\sigma_s \to 0$ m^{-1}, $\lambda_s = 0.5$ s^{-1}, $v_z = 0$ m/s
II	$\sigma_s = 0.01$ m^{-1}, $\lambda_s \to 0$ s^{-1}, $v_z = 0$ m/s
III	$\sigma_s = 0.01$ m^{-1}, $\lambda_s = 0.5$ s^{-1}, $v_z = 0$ m/s
IV	$\sigma_s = 0.05$ m^{-1}, $\lambda_s = 1$ s^{-1}, $v_z = 2$ m/s

2) Time-Varying Doppler PSD: Similar to the case in reference model, the time-varying Doppler PSD of the simulation model is obtained by applying Fourier transformation to the simulated ST-CF, i.e.,

$$\tilde{S}_{pq,p'qp}(t,\nu) = \mathcal{F}_{\Delta t}\{\tilde{\rho}_{qp,p'q'}(t,\Delta t,\Delta f=0)\}. \tag{62}$$

3) Time-Varying Delay PSD: The time-varying delay PSD of the simulation model is obtained as the inverse Fourier transform of the simulated FCF, and is written as

$$\tilde{P}_{pq,p'q'}(t,\tau) = \mathcal{F}_{\Delta f}^{-1}\{\tilde{\rho}_{qp,p'q'}(t,\Delta t=0,\Delta f)\}. \tag{63}$$

4) Stationary Interval: Analogous to the reference mode, the stationary interval of the simulation model can be estimated based on (50) and (51) by substituting $S_{pq,p'q'}(t_i,\nu)$ and $S_{pq,p'q'}(t_i+\Delta t,\nu)$ with $\tilde{S}_{pq,p'q'}(t_i,\nu)$ and $\tilde{S}_{pq,p'q'}(t_i+\Delta t,\nu)$, respectively.

V. RESULTS AND ANALYSIS

In this section, numerical results are illustrated according to the derived expressions in Sections III and IV. Statistics of reference and simulation models as well as simulation results are presented and investigated for different degrees of trajectory randomness. Unless otherwise specified, the parameters used for the simulations are: $f_c = 2$ GHz, $D = 180$ m, $H_T = 120$ m, $R_{\min} = 3$ m, $R_{\max} = 30$ m, $\delta_{T(R)} = \lambda/2$, $\gamma_{T(R)} = \pi/2$, $\varphi_R = \pi/6$, $v_{T,xy} = 15$ m/s, $v_{T,z} = 0$ m/s, $v_R = 1$ m/s, $\phi_T(t_0) = 0$, $\phi_R = \pi/3$, $\kappa = 3$, $\alpha_\mu = 2\pi/3$ $\beta_m = \pi/6$, and $K = 0$. In addition, four UAV trajectories with the same time interval [0, 10 s] but different degrees of randomness are used for testing. The parameters of Trajectory I are set as $\sigma_s \to 0$ m^{-1}, $\lambda_s = 0.5$ s^{-1}. This implies infinite turning radii and leads to a nearly straight line trajectory. In the case of the second trajectory, the parameters are set as $\sigma_s = 0.01$ m^{-1}, $\lambda_s \to 0$ s^{-1}, which results in an anticlockwise circular movement of the aircraft. Compared with the first two trajectories, Trajectory III has a higher degree of randomness by setting the parameters as $\sigma_s = 0.01$ m^{-1}, $\lambda_s = 0.5$ s^{-1}. This means the trajectories are randomly determined by a series of turning radii $r(T_i)$ and travel time intervals τ_i. Trajectory IV is set with the highest randomness by chosen the following parameters as $\sigma_s = 0.05$ m^{-1}, $\lambda_s = 1$ s^{-1}. Besides, in Trajectory I–III, the aircraft is assumed to move in the horizontal plane. For Trajectory IV, the aircraft has a vertical speed by setting $v_z = 2$ m/s. For clarity, Trajectory I–IV are shown in Fig. 4(a)–(d), respectively. Parameters used for generating those trajectories are collected in Table III. By setting appropriate RMM parameters, the generated trajectories can capture the movement patterns associated with different

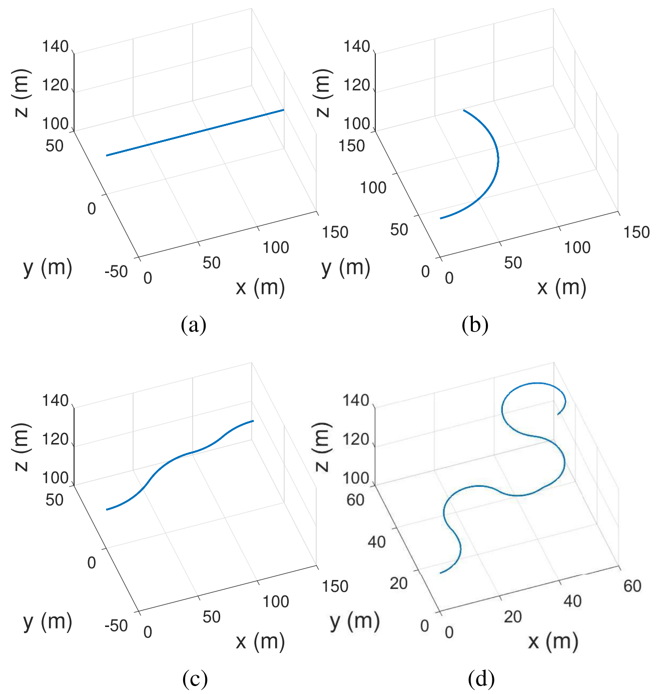

Fig. 4. Different UAV trajectories according to the parameters in Table III. (a) Trajectory I. (b) Trajectory II. (c) Trajectory III. (d) Trajectory IV.

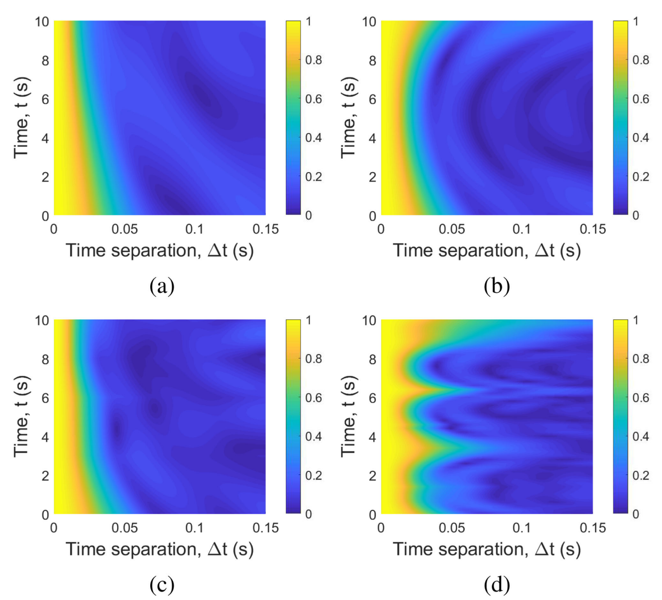

Fig. 5. Time-evolutions of the temporal ACFs of the simulation channel model for different trajectories of the UAV. (a) Trajectory I. (b) Trajectory II. (c) Trajectory III. (d) Trajectory IV.

UAV application, e.g., transportation, search and rescue, and patrolling and reconnaissance.

Fig. 5 presents the temporal autocorrelation functions (ACFs) of the proposed simulation model when the aircraft is moving along the different trajectories. The temporal ACFs are obtained by setting $p = p'$, $q = q'$, and $\Delta f = 0$ in (40). From the results, we find that even for the linear trajectory case, i.e., Fig. 5(a), the temporal ACF still varies substantially over time. This is in contrast to those of stationary channel models, in which the statistics are constant over time [13], [14], [17], [18]. The time-variation of the temporal ACFs is caused by time-varying departure and arrival angles of MPCs due to the movements of the UAV and GS. For Trajectory II, we find that the temporal correlation decreases faster and then slower along time. This is apparently affected by the linear variation of the heading direction when the aircraft move along the circular trajectory. In Fig. 5(c) and (d), the temporal ACFs vary more frequently as the randomness of trajectory increases. The significant variations of the temporal ACFs in Fig. 5(d) stem from small turning radii and fast changes of turning centers due to large values of σ_s and λ_s.

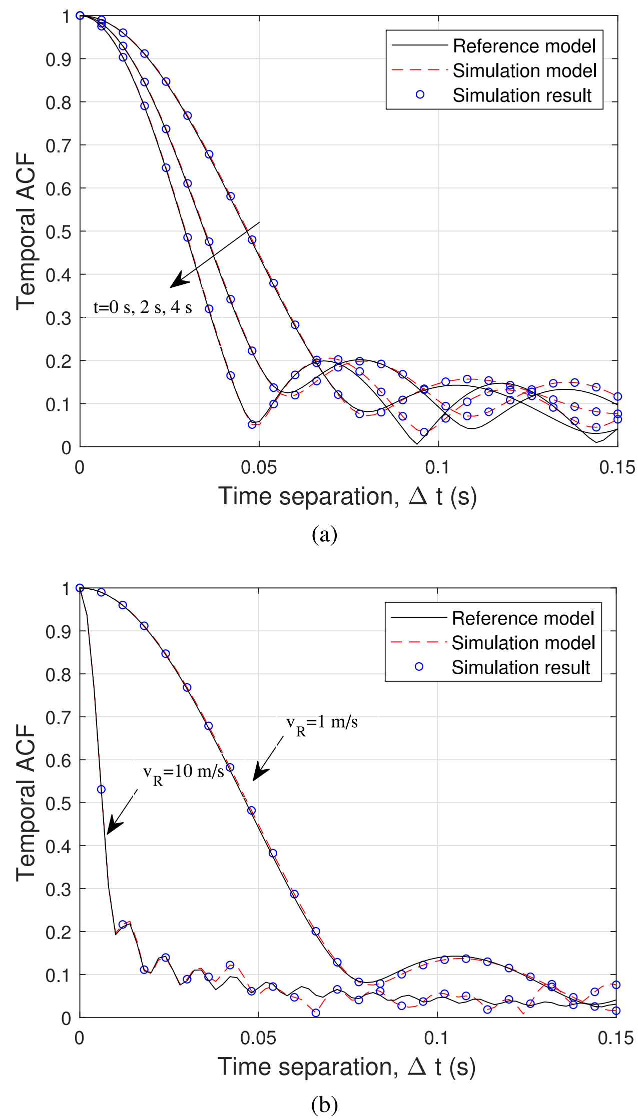

Fig. 6. Temporal ACFs for Trajectory III (a) at different time instants and (b) with different speeds of the GS.

Fig. 6(a) shows the temporal ACFs of the reference model, simulation model, and simulation results for Trajectory III, at 0 s, 2 s, and 4 s. The simulation results are generated from samples

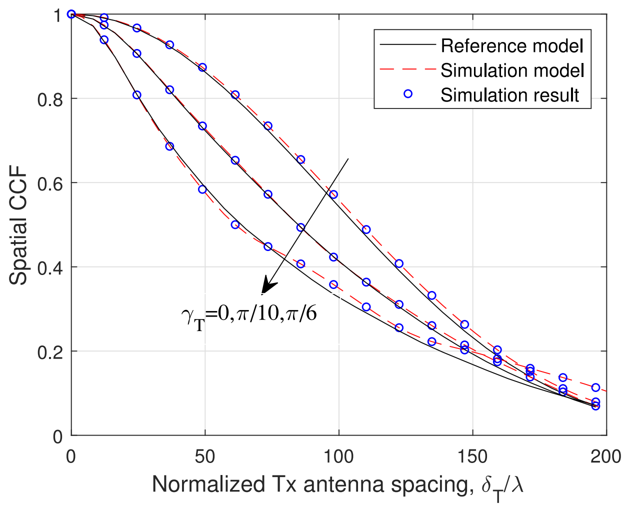

(a)

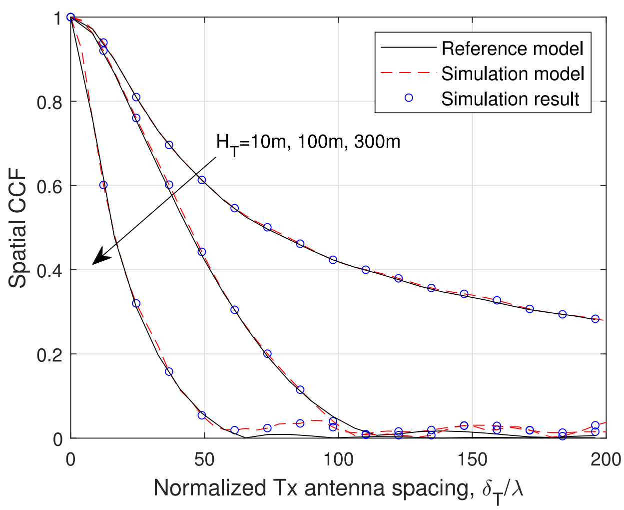

(b)

Fig. 7. Spatial CCFs for Trajectory III (a) with different tilt angles of the UAV antenna array and (b) with different altitudes of the UAV.

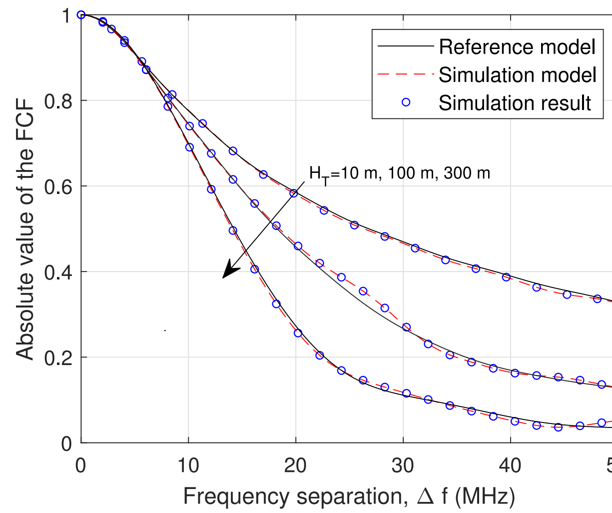

Fig. 8. FCFs for different altitudes of the UAV.

of impulse response generated by the simulation model. The temporal correlation decreases over time due to the dynamic movements of the aircraft and GS. A good agreement among reference model, simulation model, and simulation result shows the correctness our derivations. Furthermore, the impacts of GS speed on the temporal correlation of the model are presented in Fig. 6(b). In the simulation, GS velocity is set as 1 m/s and 10 m/s, which correspond to the speeds of hand-held and vehicle terminals, respectively. Since a large number of local scatterers, e.g., buildings, lampposts, trees, etc., are located around the GS and relatively far from the aircraft, higher speeds of the GS result in larger variations of the AoAs and make the temporal correlation of the channel decorrelate faster.

Fig. 7(a) shows the spatial cross-correlation functions (CCFs) for different orientations of the UAV antenna array. Here, the spatial CCFs are obtained by setting $\Delta t = 0$ and $\Delta f = 0$ in (40). The antenna spacings have been normalized against the wavelength. The results suggest that the channel has a lower spatial correlation as the tile angle of the UAV antenna array increase, which results in a larger diversity gain. Furthermore, Fig. 7(b) presented the spatial CCF when the UAV stays at different altitudes. It indicates that apart from adjusting the array orientation, a larger diversity gains can be achieved when the aircraft is flying at a higher altitude. This is because that a higher altitude of the UAV can lead to larger elevation angular spreads, which result in lower spatial correlations of the channel.

The FCFs for different altitudes of the UAV are presented in Fig. 8. Here, the result is obtained by setting $\Delta t = 0, p = p'$ and $q = q'$ in (40). It is indicated that higher UAV altitudes results in lower frequency correlation of the channel. The coherence bandwidth can be defined as the largest frequency separation during which the FCF over a threshold, i.e., 0.5 [42]. Following this definition, the coherence bandwidth of the proposed model is about 18.18 MHz when the UAV is flying at 10 m. Furthermore, a higher altitude of the UAV causes a smaller coherence bandwidth, which translates into a larger root-mean-square (RMS) delay spread. Those results are consistent with the channel measurement results [43].

Fig. 9 presents the time-varying normalized Doppler PSDs of the simulation model for Trajectories I–IV. For the case of the first trajectory, where the UAV moves with a constant heading direction, the Doppler PSD is still time-varying, indicating non-stationarity of the model in time domain, which is different from those of the stationary channel models. In Fig. 9(b), the Doppler PSD shifts to larger values over time due to the linear variation of the UAV heading direction. Besides, compared with the case of Trajectory I, slight variation of the Doppler PSD over time is illustrated in Fig. 9(c). This is resulted from larger value of σ_s. Furthermore, the time variation of the Doppler PSD is substantially intensified in Fig. 9(d) when both σ_s and λ_s are increased as $\sigma_s = 0.05\ \mathrm{m}^{-1}$, $\lambda_s = 1\ \mathrm{s}^{-1}$. The large variation of the Doppler PSD over time is caused by the high degree of trajectory randomness, which further increases temporal non-stationarity of the model.

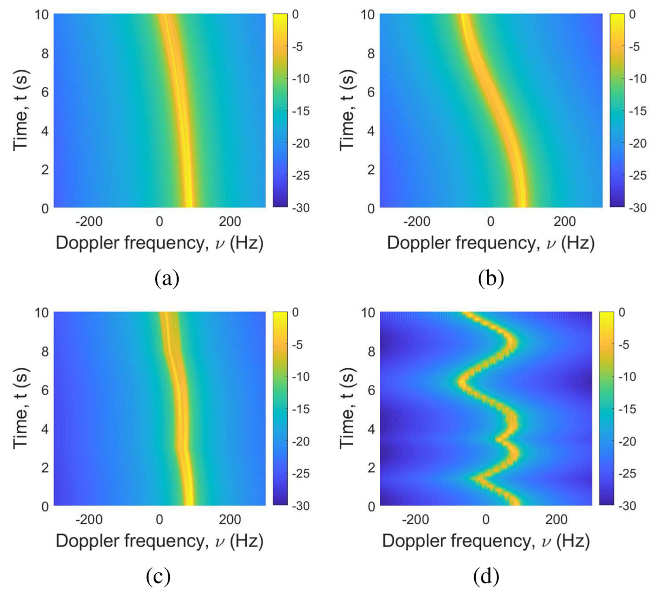

Fig. 9. Time-evolutions of normalized Doppler PSDs of the simulation model assuming various trajectories of the UAV. (a) Trajectory I. (b) Trajectory II. (c) Trajectory III. (d) Trajectory IV.

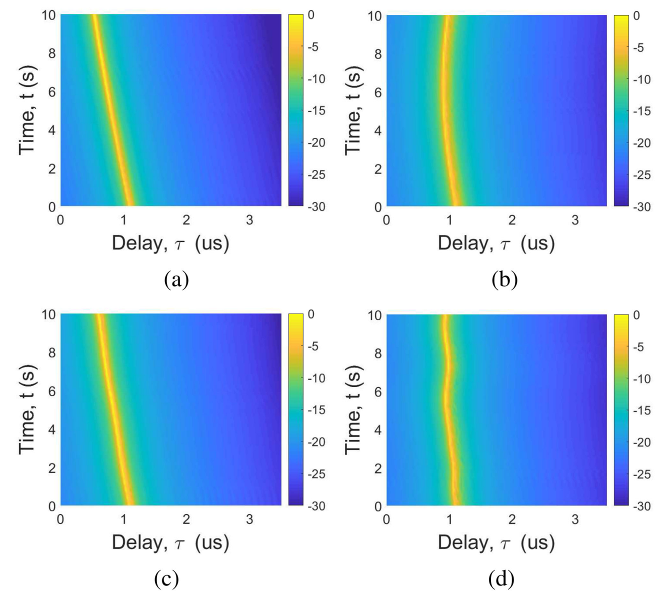

Fig. 11. Time-evolutions of normalized delay PSDs of the simulation model assuming various trajectories of the UAV. (a) Trajectory I. (b) Trajectory II. (c) Trajectory III. (d) Trajectory IV.

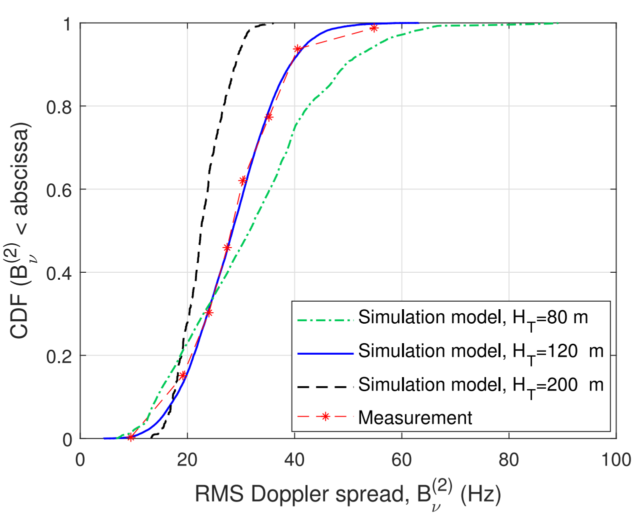

Fig. 10. CDFs of RMS Doppler spreads of the simulation model with different altitudes of the UAV and the measurement data in [44].

Fig. 10 shows the cumulative distribution functions (CDFs) of RMS Doppler spreads of the simulation model and the corresponding measurement data [44]. The measurement campaign was conducted in a residential environment. The following model parameters are selected to fit the measurement data: $f_c = 5.8$ GHz, $R_{\text{min}} = 3$ m, $R_{\text{max}} = 70$ m, $\alpha_\mu = 2\pi/3$, $\kappa = 3$, $\beta_m = \pi/6$, $\phi_T = 0$, and $K = 0.1$. Before analysis, the principle of parameter selection needs to be clarified. Parameters including carrier frequency, Tx-Rx separation, UAV altitude, and GS and UAV speeds are set according to the measurement campaigns. Other parameters are set according to communication environments or based on the relationship between model parameters and channel characteristics. For example, decreasing κ resulting in a more isotropic scattering environment and a large Doppler spread can be obtained. Note that those parameters should be adjusted or optimized to fit to measurement data. In this figure, the consistency between the proposed model and the measurement data is presented, showing the practicability of the model. Furthermore, we find that the Doppler spread becomes larger when the UAV flies at a lower altitude. The reason is that largely different AoDs can be generated due to the short travel distances between the UAV and GS surroundings, which result in very different Doppler shifts. On the contrary, when the UAV stays at a higher altitude, the travel distances from the UAV to GS surroundings become larger. The waves transmitted from UAV experiences similar Doppler shifts due to similar departure angles, leading to a smaller Doppler spread.

Fig. 11 illustrates the time-evolution of the normalized delay PSDs of the simulation model for different trajectories of the aircraft. Specifically, Fig. 11(a) and (c) illustrate the delay PSDs for linear and low randomness trajectories cases. As the UAV approaches the GS/scatterers, the the delays of MPCs decrease monotonically during the observation period. However, in Fig. 11(d), the delays of MPCs randomly varies due to high level of UAV trajectory randomness. For the circular trajectory scenario, which is given by Fig. 11(b), delays of MPCs first decrease over time when the UAV approaches the GS/scatterers and then increase as the distances between UAV and GS/scatterers become larger. The results indicate that the proposed model is able to capture the impacts of trajectory variations on delay PSDs of the UAV channel.

Fig. 12 presents the stationary intervals of the simulation model with various UAV trajectories. Each result is the average of stationary intervals associated with 10 trajectories randomly generated according to certain values of RMM parameters, i.e., λ_s and σ_s. For the case when $\lambda_s = 0.5$ s^{-1} and $\sigma_s = 0.01$ m^{-1},

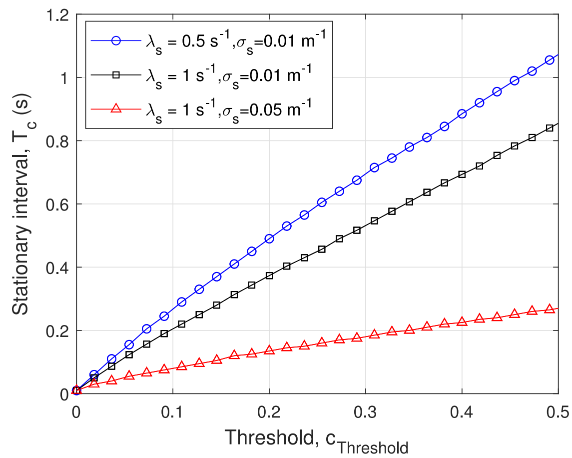

Fig. 12. Stationary intervals of the simulation model with different degrees of UAV trajectory randomness.

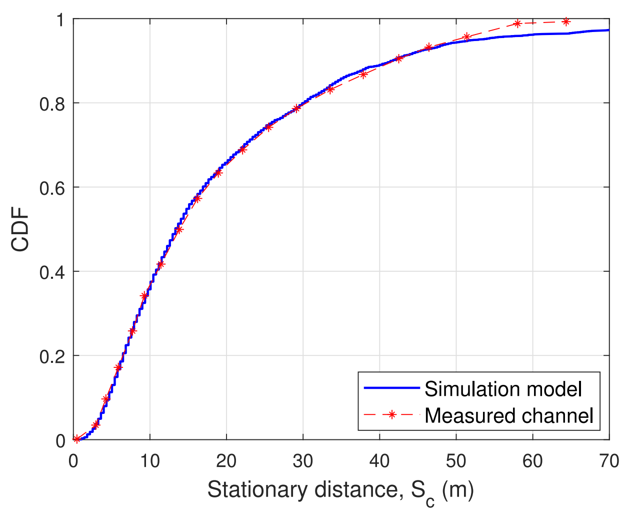

Fig. 13. CDF of stationary distance of the simulation model and measurement data in [45].

the UAV flies along nearly straight trajectories, leading to the largest stationary interval among the four cases, i.e., 0.49 s with $c_{\text{Threshold}} = 0.2$. This is equivalent to a 7.35 m stationary distance, which is close to the measurement results in [11]. When λ_s increases to 1 s^{-1}, under the same threshold, the stationary interval of the model reduces to 0.37 s. This means a larger value of λ_s can increase the non-stationarity of the channel due to fast changes of turning center. When both λ_s and σ_s increase, i.e., $\lambda_s = 1$ s^{-1} and $\sigma_s = 0.05$ m^{-1}, the stationary interval further reduces to 0.14 s for $c_{\text{Threshold}} = 0.2$, which are much shorter compared with those in former cases. The underlying reason is that a highly dynamic trajectory leads to fast-changing model parameters and statistical properties, e.g., heading direction of UAV, AoAs and AoDs of MPCs, and Doppler PSD. In (51), the similarity of the channel at different time, i.e., $d_{\text{DPSD}}(t_i, \Delta t)$, can exceed c_{thresh} within a shorter Δt. The results indicate that the proposed stationary interval metric is useful for capturing the channel non-stationarity resulted from dynamic UAV movements.

Fig. 13 compares the CDF of stationary distances of the proposed simulation model with measured channel [45]. The measurements were carried out at 5.06 GHz in the over-sea environment near Oxnard, CA. The aircraft flies at a speed of 90 m/s along a straight track and the altitude is about 800 m. According to the measurement campaigns, the following parameters are chosen for the simulation model: $f_c = 5.06$ GHz, $R_{\min} = 30$ m, $R_{\max} = 300$ m, $D = 12$ km, $H_T = 800$ m, $v_{T,xy} = 90$ m/s, $v_{T,z} = 0$ m/s, $K = 31$ dB, $\sigma_s = 10^{-5}$ m^{-1}, and $\lambda_s = 0.5$ s^{-1}. The stationary distance is estimated by temporal PDP correlation coefficient (TPCC) method [40] and can be translated into stationary interval by $T_c = S_c/v_{T,xy}$. A good match between the proposed model and measurement is shown, validating the ability of the model in capturing temporal non-stationarity of UAV channels.

VI. Conclusion

In this paper, we relax the widely used straight-line trajectory condition in UAV channel modeling and present a temporally non-stationary wideband MIMO UAV-to-ground channel model. This was achieved by incorporating the aeronautic ST-RMM into a geometrical concentric-cylinders model, making the model more general and adaptable to various UAV communication scenarios. Based on the motions of the UAV and GS, time-varying model parameters have been derived. Statistics including STF-CF, Doppler PSD, and delay PSD have been obtained and analyzed in terms of different UAV trajectories. A novel stationary interval metric has been proposed, which has been shown to be useful to estimate the temporal non-stationarity of the UAV channel resulting from dynamic trajectories (due to variations of moving direction). Results have indicated that the dynamic UAV trajectories can exert substantially influences on channel characteristics and increase the temporal non-stationarity of the channel. The reference model and simulation model have been compared with the corresponding simulation results, indicating the fidelity of the derivations. The practicability of the model has been verified by measurement data with respect to RMS Doppler spread and stationary interval. The proposed model can be extended to mmWave or THz bands by properly adjusting model parameters and adding necessary channel properties, e.g., blockage effect, oxygen absorption, and frequency dependence [46], [47]. Besides, directional antennas are often adopted in mmWave communication to compensate for severe pathloss [48]. In the proposed model, the effects of directional antennas on UAV channels can be simulated by eliminating the scatterers outside the main lobe of antenna patterns.

References

[1] X.-H. You *et al.*, "Towards 6G wireless communication networks: Vision, enabling technologies, and new paradigm shifts," *Sci. China Inf. Sci*, vol. 64, no. 1, pp. 1–74, Jan. 2021, doi: 10.1007/s11432-020-2955-6.

[2] C.-X. Wang, J. Huang, H. M. Wang, X. Q. Gao, X. H. You, and Y. Hao, "6G wireless channel measurements and models: Trends and challenges," *IEEE Veh. Technol. Mag.*, vol. 15, no. 4, pp. 22–32, Dec. 2020.

[3] W. Khawaja, I. Guvenc, D. W. Matolak, U. Fiebig, and N. Schneckenburger, "A survey of air-to-ground propagation channel modeling for unmanned aerial vehicles," *IEEE Commun. Surv. Tuts.*, vol. 21, no. 3, pp. 2361–2391, Jul.–Sep. 2019.

[4] Y. Liu, C.-X. Wang, H. Chang, Y. He, and J. Bian, "A novel non-stationary 6G UAV channel model for maritime communications," *IEEE J. Sel. Areas Commun.*, vol. 39, no. 10, pp. 2992–3005, Oct. 2021.

[5] E. Greenberg and P. Levy, "Channel characteristics of UAV to ground links over multipath urban environments," in *Proc. IEEE Int. Conf. Microw., Antennas, Commun. Electron. Syst.*, Tel-Aviv, Israel, 2017, pp. 1–4.

[6] C. Calvo-Ramírez, Z. Cui, C. Briso, K. Guan, and D. W. Matolak, "UAV air-ground channel ray tracing simulation validation," in *Proc. IEEE Int. Conf. Commun. China*, Beijing, China, 2018, pp. 122–125.

[7] Z. Gao, B. Liu, Z. Cheng, C. Chen, and L. Huang, "Marine mobile wireless channel modeling based on improved spatial partitioning ray tracing," *China Commun.*, vol. 17, no. 3, pp. 1–11, Mar. 2020.

[8] C.-X. Wang, J. Bian, J. Sun, W. Zhang, and M. Zhang, "A survey of 5G channel measurements and models," *IEEE Commun. Surv. Tuts.*, vol. 20, no. 4, pp. 3142–3168, Oct.–Dec. 2018.

[9] R. Sun and D. W. Matolak, "Air-ground channel characterization for unmanned aircraft systems Part II: Hilly and mountainous settings," *IEEE Trans. Veh. Technol.*, vol. 66, no. 3, pp. 1913–1925, Mar. 2017.

[10] D. W. Matolak and R. Sun, "Air-ground channel characterization for unmanned aircraft systems - Part III: The suburban and near-urban environments," *IEEE Trans. Veh. Technol.*, vol. 66, no. 8, pp. 6607–6618, Aug. 2017.

[11] D. W. Matolak and R. Sun, "Air-ground channel characterization for unmanned aircraft systems-Part I: Methods, measurements, and models for over-water settings," *IEEE Trans. Veh. Technol.*, vol. 66, no. 1, pp. 26–44, Jan. 2017.

[12] M. Simunek, F. P. Fontán, and P. Pechac, "The UAV low elevation propagation channel in urban areas: Statistical analysis and time-series generator," *IEEE Trans. Antennas Propag.*, vol. 61, no. 7, pp. 3850–3858, Jul. 2013.

[13] R. Jia, Y. Li, X. Cheng, and B. Ai, "3D geometry-based UAV-MIMO channel modeling and simulation," *China Commun.*, vol. 15, no. 12, pp. 64–74, Dec. 2018.

[14] E. T. Michailidis and A. G. Kanatas, "Three-dimensional HAP-MIMO channels: Modeling and analysis of space-time correlation," *IEEE Trans. Veh. Technol.*, vol. 59, no. 5, pp. 2232–2242, Jun. 2010.

[15] L. Zeng, X. Cheng, C.-X. Wang, and X. Yin, "A 3D geometry-based stochastic channel model for UAV-MIMO channels," in *Proc. IEEE Wireless Commun. Netw. Conf.*, San Francisco, CA, USA, 2017, pp. 1–5.

[16] H. Jiang, Z. Zhang, L. Wu, and J. Dang, "Three-dimensional geometry-based UAV-MIMO channel modeling for A2G communication environments," *IEEE Commun. Lett.*, vol. 22, no. 7, pp. 1438–1441, Jul. 2018.

[17] S. M. Gulfam, J. Syed, M. N. Patwary, and M. Abdel-Maguid, "On the spatial characterization of 3D air-to-ground radio communication channels," in *Proc. IEEE Int. Conf. Commun.*, 2015, pp. 2924–2930.

[18] X. Cheng, Y. Li, C.-X. Wang, X. Yin, and D. W. Matolak, "A 3D geometry-based stochastic model for unmanned aerial vehicle MIMO Ricean fading channels," *IEEE Internet Things J.*, vol. 7, no. 9, pp. 8674–8687, Sep. 2020.

[19] X. Zhang and X. Cheng, "Second order statistics of simulation models for UAV-MIMO Ricean fading channels," in *Proc. IEEE Int. Conf. Commun.*, Shanghai, China, 2019, pp. 1–6.

[20] J. Wang, C.-X. Wang, J. Huang, H. Wang, and X. Gao, "A general 3D space-time-frequency non-stationary THz channel model for 6G ultra-massive MIMO wireless communication systems," *IEEE J. Sel. Areas Commun.*, vol. 39, no. 6, pp. 1576–1589, Jun. 2021.

[21] X. Cheng and Y. Li, "A 3D geometry-based stochastic model for UAV-MIMO wideband nonstationary channels," *IEEE Internet Things J.*, vol. 6, no. 2, pp. 1654–1662, Apr. 2019.

[22] H. Chang, J. Bian, C. Wang, Z. Bai, W. Zhou, and E. M. Aggoune, "A 3D non-stationary wideband GBSM for low-altitude UAV-to-ground V2V MIMO channels," *IEEE Access*, vol. 7, pp. 70 719–70732, 2019, doi: 10.1109/ACCESS.2019.2919790.

[23] E. T. Michailidis, N. Nomikos, P. Trakadas, and A. G. Kanatas, "Three-dimensional modeling of mmWave doubly massive MIMO aerial fading channels," *IEEE Trans. Veh. Technol.*, vol. 69, no. 2, pp. 1190–1202, Feb. 2020.

[24] H. Chang *et al.*, "A novel non-stationary 6G UAV-to-ground wireless channel model with 3D arbitrary trajectory changes," *IEEE Internet Thing J.*, vol. 8, no. 12, pp. 9865–9877, Jun. 2021.

[25] Z. Ma, B. Ai, R. He, G. Wang, Y. Niu, and Z. Zhong, "A wideband non-stationary air-to-air channel model for UAV communications," *IEEE Trans. Veh. Technol.*, vol. 69, no. 2, pp. 1214–1226, Feb. 2020.

[26] W. Dahech, M. Pätzold, C. A. Gutiérrez, and N. Youssef, "A non-stationary mobile-to-mobile channel model allowing for velocity and trajectory variations of the mobile stations," *IEEE Trans. Wireless Commun.*, vol. 16, no. 3, pp. 1987–2000, Mar. 2017.

[27] T. Camp, J. Boleng, and V. Davies, "A survey of mobility models for ad hoc network research," *Wireless Commun. Mobile Comput.*, vol. 2, no. 5, pp. 483–502, Aug. 2002.

[28] R. He, B. Ai, G. L. Stüber, and Z. Zhong, "Mobility model-based non-stationary mobile-to-mobile channel modeling," *IEEE Trans. Wireless Commun.*, vol. 17, no. 7, pp. 4388–4400, Jul. 2018.

[29] Y. Wan, K. Namuduri, Y. Zhou, and S. Fu, "A smooth-turn mobility model for airborne networks," *IEEE Trans. Veh. Technol.*, vol. 62, no. 7, pp. 3359–3370, Sep. 2013.

[30] N. Nabaa and R. H. Bishop, "Validation and comparison of coordinated turn aircraft maneuver models," *IEEE Trans. Aerosp. Electron. Syst.*, vol. 36, no. 1, pp. 250–259, Jan. 2000.

[31] X. R. Li and V. P. Jilkov, "Survey of maneuvering target tracking: Part I. Dynamic models," *IEEE Trans. Aerosp. Electron. Syst.*, vol. 39, no. 4, pp. 1333–1364, Oct. 2003.

[32] J. Xie, Y. Wan, K. Namuduri, S. Fu, G. L. Peterson, and J. F. Raquet, "Estimation and validation of the 3D smooth-turn mobility model for airborne networks," in *Proc. IEEE Mil. Commun. Conf.*, 2013, pp. 556–561.

[33] J. Bian *et al.*, "A 3D wideband non-stationary multi-mobility model for vehicle-to-vehicle MIMO channels," *IEEE Access*, vol. 7, pp. 32 562–32 577, 2019, doi: 10.1109/ACCESS.2019.2901805.

[34] S. Wu, C.-X. Wang, e. H. M. Aggoune, M. M. Alwakeel, and X. H. You, "A general 3D non-stationary 5G wireless channel model," *IEEE Trans. Commun.*, vol. 66, no. 7, pp. 3065–3078, Jul. 2018.

[35] A. Abdi, J. A. Barger, and M. Kaveh, "A parametric model for the distribution of the angle of arrival and the associated correlation function and power spectrum at the mobile station," *IEEE Trans. Veh. Technol.*, vol. 51, no. 3, pp. 425–434, May 2002.

[36] J. D. Parsons and A. M. D. Turkmani, "Characterisation of mobile radio signals: Model description," *IEE Proc. I - Commun., Speech Vis.*, vol. 138, no. 6, pp. 549–556, Dec. 1991.

[37] A. G. Zajić, G. L. Stüber, T. G. Pratt, and S. T. Nguyen, "Wideband MIMO mobile-to-mobile channels: Geometry-based statistical modeling with experimental verification," *IEEE Trans. Veh. Technol.*, vol. 58, no. 2, pp. 517–534, Feb. 2009.

[38] J. Bian, C.-X. Wang, X. Q. Gao, X. H. You, and M. G. Zhang, "A general 3D non-stationary wireless channel model for 5G and beyond," *IEEE Trans. Wireless Commun.*, vol. 20, no. 5, pp. 3211–3224, May 2021.

[39] M. Herdin, N. Czink, H. Ozcelik, and E. Bonek, "Correlation matrix distance, a meaningful measure for evaluation of non-stationary MIMO channels," in *Proc. IEEE Veh. Technol. Conf.*, Stockholm, Sweden, May 2005, pp. 136–140.

[40] A. Gehring, M. Steinbauer, I. Gaspard, and M. Grigat, "Empirical channel stationarity in urban environments," in *Proc. 4th Eur. Pers. Mobile Commun. Conf.*, Vienna, Austria, 2001, pp. 1–6.

[41] C. A. Gutiérrez and M. Pätzold, "Sum-of-sinusoids-based simulation of flat fading wireless propagation channels under non-isotropic scattering conditions," in *Proc. IEEE Glob. Telecommun. Conf.*, Washington, DC, USA, 2007, pp. 3842–3846.

[42] A. F. Molisch, *Wireless Communications*, 2nd ed. Hoboken, NJ, USA: Wiley, 2010.

[43] W. Khawaja, I. Guvenc, and D. Matolak, "UWB channel sounding and modeling for UAV air-to-ground propagation channels," in *Proc. IEEE Glob. Commun. Conf.*, Washington, USA, 2016, pp. 1–7.

[44] R. M. Gutierrez, H. Yu, Y. Rong, and D. W. Bliss, "Time and frequency dispersion characteristics of the UAS wireless channel in residential and mountainous desert terrains," in *Proc. IEEE Annu. Consum. Netw. Conf.*, Las Vegas, USA, 2017, pp. 516–521.

[45] D. W. Matolak and R. Sun, "Antenna and frequency diversity in the unmanned aircraft systems bands for the over-sea setting," in *Proc. IEEE/AIAA Digit. Avionics Syst. Conf.*, Colorado Springs, CO, USA, 2014, pp. 6A4-1–6A4-10.

[46] J. Wang *et al.*, "A novel 3D non-stationary GBSM for 6G THz ultra massive MIMO wireless systems," *IEEE Trans. Veh. Technol.*, to be published, doi: 10.1109/TVT.2021.3117239.

[47] Y. Tan, C.-X. Wang, J. Ø. Nielsen, G. F. Pedersen, and Q. Zhu, "A novel B5G frequency non-stationary wireless channel model," *IEEE Trans. Antennas Propag.*, vol. 69, no. 8, pp. 4846–4860, Aug. 2021.

[48] R. He, B. Ai, G. L. Stüber, G. Wang, and Z. Zhong, "Geometrical-based modeling for millimeter-wave MIMO mobile-to-mobile channels," *IEEE Trans. Veh. Technol.*, vol. 67, no. 4, pp. 2848–2863, Apr. 2018.

Ji Bian (Member, IEEE) received the B.Sc. degree in electronic information science and technology from Shandong Normal University, Jinan, Chian, in 2010, the M.Sc. degree in signal and information processing from the Nanjing University of Posts and Telecommunications, Nanjing, China, in 2013, and the Ph.D. degree in information and communication engineering from Shandong University, Jinan, China, in 2019. From 2017 to 2018, he was a Visiting Scholar with the School of Engineering and Physical Sciences, Heriot-Watt University, Edinburgh, U.K. He is currently a Lecturer with the School of Information Science and Engineering, Shandong Normal University, Jinan, China. His research interests include 6G channel modeling and wireless Big Data.

Cheng-Xiang Wang (Fellow, IEEE) received the B.Sc. and M.Eng. degrees in communication and information systems from Shandong University, Jinan, China, in 1997 and 2000, respectively, and the Ph.D. degree in wireless communications from Aalborg University, Aalborg, Denmark, in 2004.

He was a Research Assistant with the Hamburg University of Technology, Hamburg, Germany, from 2000 to 2001, a Visiting Researcher with Siemens AG Mobile Phones, Munich, Germany, in 2004, and a Research Fellow with the University of Agder, Grimstad, Norway, from 2001 to 2005. He has been with Heriot-Watt University, Edinburgh, U.K., since 2005, where he was promoted to a Professor in 2011. In 2018, he joined Southeast University, Nanjing, China, as a Professor. He is also a part-time Professor with Purple Mountain Laboratories, Nanjing. He has authored four books, three book chapters, and more than 430 papers in refereed journals and conference proceedings, including 25 highly cited papers. He has also delivered 22 invited keynote speeches/talks and nine tutorials in international conferences. His research interests include wireless channel measurements and modeling, 6G wireless communication networks, and applying artificial intelligence to wireless communication networks.

Dr. Wang is a Member of the Academia Europaea (The Academy of Europe), a Fellow of the IET, and China Institute of Communication (CIC), an IEEE Communications Society Distinguished Lecturer in 2019 and 2020, and a Highly-Cited Researcher recognized by Clarivate Analytics in 2017–2020. He is currently an Executive Editorial Committee Member of the IEEE Transactions on Wireless Communications. He was the Editor of nine international journals, including IEEE Transactions on Wireless Communications, from 2007 to 2009, IEEE Transactions on Vehicular Technology, from 2011 to 2017, and IEEE Transactions on Communications, from 2015 to 2017. He was the Guest Editor of IEEE Journal on Selected Areas in Communications, Special Issue on Vehicular Communications and Networks (Lead Guest Editor), Special Issue on Spectrum and Energy Efficient Design of Wireless Communication Networks, and Special Issue on Airborne Communication Networks. He was also the Guest Editor of IEEE Transactions on Big Data, Special Issue on Wireless Big Data, and is the Guest Editor of IEEE Transactions on Cognitive Communications and networking, Special Issue on Intelligent Resource Management for 5G and Beyond. He was a TPC Member, TPC Chair, and the General Chair for more than 80 international conferences. He was the recipient of 12 best paper awards from IEEE GLOBECOM 2010, IEEE ICCT 2011, ITST 2012, IEEE VTC 2013-Spring, IWCMC 2015, IWCMC 2016, IEEE/CIC ICCC 2016, WPMC 2016, WOCC 2019, IWCMC 2020, and WCSP 2020. Also, he was the recipient of 2020 & 2021 AI 2000 Most Influential Scholar Award Honourable Mention in recognition of his outstanding and vibrant contributions in the field of Internet of Things.

Yu Liu (Member, IEEE) received the Ph.D. degree in communication and information systems from Shandong University, Jinan, China, in 2017. From 2015 to 2017, she was a Visiting Scholar with the School of Engineering and Physical Sciences, Heriot-Watt University, Edinburgh, U.K. From 2017 to 2019, she was a Postdoctoral Research Associate with the School of Information Science and Engineering, Shandong University, Jinan, China. Since 2019, she has been an Associate Professor with the School of Microelectronics, Shandong University, Jinan, China. Her research interests include nonstationary wireless MIMO channel modeling, high speed train wireless propagation characterization and modeling, and channel modeling for special scenarios.

Jie Tian (Member, IEEE) received the B.E. and M.E. degrees from Shandong Normal University, China, in 2008 and 2011, respectively, and the Ph.D. degree in communication and information systems from the School of Information Science and Engineering, Shandong University, China, in 2016. She is currently an Associate Professor with the School of Information Science and Engineering, Shandong Normal University, Jinan, China. Her research interests include cross-layer design of wireless communication networks, radio resource management in heterogeneous networks, and signal processing for communications.

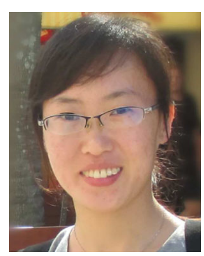

Jingping Qiao (Member, IEEE) received the B.E. degree from the School of Information Engineering, Inner Mongolia University of Science & Technology, China, in 2012 and the Ph.D. degree from Shandong University, China, in 2018. She is currently a Lecturer with the School of Information Science and Engineering, Shandong Normal University, China. Her research interests include physical layer security, cooperative (relay) systems, terahertz communications, signal processing for communications, and simultaneous wireless information and power transfer.

Xiangwei Zheng is currently a Professor with the School of Information Science and Engineering, Shandong Normal University, China. His research interests include cloud computing, computer networks and computational intelligence etc. He was involved in several national natural science foundation of China and is author of more than 60 national and international publications in conferences and journals.